BMC Biotechnology

RESEARCH

Open Access

Anticancer effects of bisabolol oxide A-Loaded Micellar/Liposomal nanoparticles on DU-145 cells with deregulation of miR-34a and miR-181a: in silico and in vitro studies

Shirin Fekri Kohan[1], Zohreh Arefi Khorrami[2], Fatemeh Bahrevar Fatideh[3], Shahin Nezamivand Chegini[1], Alireza Nouhi Kararoudi[3], Hossein Zahmatkesh[4], Behnam Rasti[3], Mohammad Nikpassand[5], Mahdi Shahriarinour[1*], Najmeh Ranji[1*] and Yavuz Nuri Ertas[6*]

Abstract

Bisabolol oxide A, a key bioactive constituent of Matricaria chamomilla, is recognized for its potent anti-inflammatory, antioxidant, and anticancer properties. This study focused on synthesizing bisabolol oxide A-loaded micellar/liposomal nanoparticles (NPs) and rigorously evaluating their anti-proliferative and anti-invasive effects using integrated in vitro and in silico methodologies. Physicochemical characterization of the bisabolol oxide A-loaded NPs was performed using SEM, TEM, TGA-DTG, Zeta potential, DLS analysis, and FT-IR spectroscopy. Furthermore, drug-like properties for bisabolol oxide A, bisabolol oxide B, and 5,8,11-heptadecatriynoic acid methyl ester were predicted using Swiss ADME software. Molecular dynamics simulations were subsequently conducted for these compounds against critical cellular migration proteins: β-catenin and the Epidermal Growth Factor Receptor (EGFR). The anticancer efficacy of the bisabolol oxide A-loaded nanoparticles was assessed through MTT assays, Annexin V/PI staining, wound healing assays, and qRT-PCR. Characterizations confirmed that the nanoparticles possessed optimal characteristics, exhibiting sizes between 35 to 67 nm, high mono-dispersity and thermal stability up to 380°C. In vitro results demonstrated that bisabolol oxide A-loaded micellar/liposomal nanoparticles significantly inhibited DU-145 cell proliferation, yielding IC_{50} value of 55.44 µg/mL, 46.21 µg/mL, and 43.59 µg/mL after 24, 48, and 72 hours of treatment. Flow-cytometry analysis further confirmed 50.04% reduced migratory capacity and induction of apoptosis. Mechanistically, qRT-PCR analysis revealed a significant 2.31 ± 0.16-fold upregulation of the tumor-suppressive miR-34a and a 1.72 ± 0.03-fold downregulation of the oncomiR miR-181a in treated cells. These miRNA alterations correlated with the downregulation of migration-associated genes (CTNNB, SMAD3, and EGFR) and the upregulation of apoptosis-related genes (P53 and CASP9), findings

*Correspondence:
Mahdi Shahriarinour
ma.shahriarinour@iau.ac.ir
Najmeh Ranji
na.ranji@iau.ac.ir
Yavuz Nuri Ertas
yavuznuri@gmail.com

Full list of author information is available at the end of the article

© The Author(s) 2026. **Open Access** This article is licensed under a Creative Commons Attribution-NonCommercial-NoDerivatives 4.0 International License, which permits any non-commercial use, sharing, distribution and reproduction in any medium or format, as long as you give appropriate credit to the original author(s) and the source, provide a link to the Creative Commons licence, and indicate if you modified the licensed material. You do not have permission under this licence to share adapted material derived from this article or parts of it. The images or other third party material in this article are included in the article's Creative Commons licence, unless indicated otherwise in a credit line to the material. If material is not included in the article's Creative Commons licence and your intended use is not permitted by statutory regulation or exceeds the permitted use, you will need to obtain permission directly from the copyright holder. To view a copy of this licence, visit http://creativecommons.org/licenses/by-nc-nd/4.0/.

substantiated by Western blot analysis. In silico analyses indicated favorable ADMET properties for bisabolol oxide A, bisabolol oxide B, and 5,8,11-heptadecatriyneoic acid methyl ester. Molecular docking simulations revealed strong binding affinities of these compounds for β-catenin and EGFR, which are key proteins in cellular migration pathways. Our findings strongly suggest that bisabolol oxide A functions as an anti-migration and pro-apoptotic agent by effectively modulating the expression of specific miRNAs and their transcriptional targets, complemented by potent inhibitory interactions with critical protein targets.

Keywords Bisabolol oxide A, Nanoparticle, Apoptosis, Molecular docking, Anti-migration, β-Catenin, EGFR

Introduction

Bisabolol oxide A ($C_{15}H_{26}O_2$) is a principal constituent of German chamomile (*Matricaria chamomilla*) [1]. Chamomile, a member of the Asteraceae family, formerly known as Compositae, is an ancient medicinal herb historically used and cultivated across Europe and Western Asia [2, 3]. This plant is renowned for a broad spectrum of medicinal properties, including anti-inflammatory, antioxidant, hepatoprotective, anticancer, antiallergic [4], antibacterial, antifungal [5], and antispasmodic activities [6]. Specifically, the antihyperalgesic and antiedematous effects of Matricaria oil, which is rich in bisabolol oxides, have been documented [7]. Furthermore, *Matricaria chamomilla L.* essential oil has notable anti-inflammatory and anticancer effects against various cancer cell lines [8]. Due to its poor aqueous solubility, recent biological investigations have focused on developing novel strategies to enhance the solubility of bisabolol oxide A in aqueous media and physiological fluids, thereby improving its therapeutic potential.

MicroRNAs (miRNAs) are recognized as critical post-transcriptional regulators of gene expression [9]. A single miRNA can target numerous mRNAs, influencing diverse stages of cellular differentiation, proliferation, and tissue development [10]. A large proportion of mature mRNAs are predicted to contain potential miRNA-binding sites. Approximately 2,600 mature miRNAs have been annotated. Dysregulation of these essential gene regulators has been implicated in the pathogenesis of various diseases, including cancer [11, 12]. miRNAs can exhibit contex-dependent dual roles: oncomiRs may promote tumorigenesis by suppressing tumor suppressor mRNAs, whereas tumor-suppressive miRNAs may inhibit oncogenic mRNAs [13]. For instance, miR-34a, a well-established tumor-suppressive miRNA, regulates several oncogenic pathways essential for cell proliferation, migration, invasion, and resistance to apoptosis [14]. Conversely, miR-181a exhibits context-dependent functions across different cancer types, targeting both oncogenes and tumor suppressor genes [15] and promoting angiogenesis [16].

Currently, diverse nanoplatforms, including micelles, liposomes, niosomes, hydrogels, polymersomes, and inorganic/polymeric nanoparticles, are employed to optimize drug delivery systems [17–28]. Research has consistently demonstrated that nanoparticle size and structure are critical determinants of therapeutic efficacy. Typically, micelles, liposomes, and polymersomes exhibit mean diameters ranging from 10 to 100 nm, 20–415 nm, and 5 nm–5 µm, respectively [29]. Micelles are formed through the self-assembly of surfactants, amphiphilic molecules, or amphiphilic block copolymers into nanoscale structures with a hydrophobic core and hydrophilic shell, whereas polymersomes are formed by the self-assembly of amphiphilic block copolymers into stable vesicular bilayer structures surrounding an aqueous core. Among these, liposomes are particularly useful for encapsulating sensitive or poorly soluble therapeutic compounds and are widely utilized across biomedical fields.

Metastasis involves a series of complex processes such as basement membrane degradation, epithelial-mesenchymal transition (EMT), tumor cell migration, and invasion, all of which are tightly orchestrated by cell adhesion molecules and associated signaling pathways [30–33]. E-cadherin-mediated signaling, involving adaptor proteins such as β-catenin and p120, plays a pivotal role in maintaining epithelial cell adhesion and regulating cell growth, migration, and plasticity [34]. Specifically, cell adhesion is mediated by the E-cadherin complex, particularly through E-cadherin/β-catenin/α-catenin interactions, while disruption of this complex can facilitate invasion [35, 36]. In poorly differentiated or aggressive tumors, the cytoplasmic and nuclear expression of E-cadherin is often diminished [37]. Furthermore, the interactions between cancer cells and the extracellular matrix can regulate apoptotic susceptibility, survival signaling, and metastatic behavior [38].

Apoptosis, or programmed cell death, is a tightly regulated process mediated by caspases, which are classified as either initiators or effectors [39, 40]. *Caspase-8* (*CASP8*) and *caspase-9* (*CASP9*) function as initiator caspases, governing the extrinsic and intrinsic apoptotic signaling pathways, respectively [41]. Specifically, *CASP8* activation within the death-inducing signaling complex directly activates *caspase-3* (*CASP3*) [42]. Within the intrinsic pathway, the release of cytochrome c and the subsequent assembly of the apoptosome with apoptotic peptidase activating factor 1 (APAF-1) are necessary for *CASP9* activation, which subsequently triggers the

proteolytic maturation of *CASP3* and initiates cellular apoptosis [43]. Given the reported bioactivity of bisabolol oxide A, the present study investigated its anticancer effects at both the transcriptional and translational levels.

A significant challenge in translating the therapeutic potential of bisabolol oxide A is its poor solubility in water and physiological fluids. To circumvent this limitation, we encapsulated bisabolol oxide A within novel micellar/liposomal nanoparticles. This formulation allowed us to evaluate the effects of the encapsulated agent at both the cellular and molecular levels in DU-145 prostate cancer cells. Building upon the known anticancer effects of chamomile components, this study also systematically evaluated the binding affinities of key bisabolol oxide A-related compounds toward two metastasis-associated proteins (β-catenin and EGFR), followed by an examination of the expression levels of these target proteins following bisabolol oxide A treatment.

Materials and methods

PEG_{400}-OA nanocarriers, were synthesized using triethylamine (TEA) (0.012 mol), oleoyl chloride (0.01 mol), and PEG400 (0.01 mol). This synthesis involved the esterification reaction between oleoyl chloride (0.01 mol) and PEG_{400} (0.01 mol) in the presence of triethylamine (0.012 mol) as the base, with chloroform serving as the solvent. This reaction was conducted under an inert atmosphere at 25 °C for 4 hours. Subsequently, the resulting triethylamine hydrochloride salt byproduct was removed from the organic phase via filtration. The final purification step involved the evaporation of chloroform from PEG_{400}-OA product in a vacuum oven at 40 °C for 4 hours [44]. Bisabolol oxide A (Sigma-Aldrich) was then encapsulated into the synthesized PEG_{400}-OA nanoparticles at a precise weight ratio of 1:5. The resulting Bisabolol oxide A-loaded PEG_{400}-OA nanoparticles exhibited solubility across varying ratios in phosphate-buffered saline (PBS). All encapsulation procedures were performed under light-protected conditions at room temperature (25°C).

Physicochemical measurements

Fourier Transform Infrared (FTIR) Spectroscopy

Fourier-transform infrared (FT-IR) spectra of the raw bisabolol oxide A, empty PEG_{400}-OA nanoparticles, and the bisabolol oxide A-loaded micellar/liposomal nanoparticles were recorded using a Shimadzu FTIR-8400S spectrometer (Shimadzu Europe).

Field-emission Scanning electron Microscopy (FE-SEM)

The morphology of the nanoparticles was examined via Field-Emission Scanning Electron Microscopy (FE-SEM). For sample preparation, a droplet of the bisabolol oxide A-loaded micellar/liposomal nanoparticle suspension (1 mg/mL) was deposited onto an adhesive carbon support film. The sample was subsequently coated with a 100 Å thick layer of gold using an ion sputtering unit (SBC-12, KYKY, China). SEM images were acquired at an accelerating voltage of 26 kV using a TESCAN microscope (Czech Republic).

Transmission electron Microscopy (TEM)

Morphology and particle size distribution were assessed using TEM using on a Zeiss-EM10C-100 kV transmission electron microscope (Germany). For TEM sample preparation, the bisabolol oxide A-loaded micellar/liposomal nanoparticle suspension (1 mg/mL) was dispersed in distilled water. A 20 µL drop of the suspension was placed onto a carbon-coated copper grid, allowed to adsorb for 2 min, blotted with filter paper to remove excess liquid, negatively stained with 2% uranyl acetate, and air-dried at room temperature prior to imaging.

Thermogravimetric analysis (TGA)

The thermal properties decomposition profile of the bisabolol oxide A-loaded micellar/liposomal nanoparticles were analyzed using a Thermogravimetric Analyzer (TGA, TA Q600, USA).

Energy-dispersive X-ray (EDX) spectrometry

The elemental composition of the bisabolol oxide A-loaded micellar/liposomal nanoparticles was analyzed using the EDX system integrated with a MIRA2 microscope (TESCAN, Czech Republic).

Stability assessment

The physical stability of the bisabolol oxide A-loaded micellar/liposomal nanoparticles was evaluated by storing two separate samples at 4 °C for one week and one year, respectively. Stability was quantified by monitoring changes in particle size, zeta-potential, and polydispersity index (PDI). Particle size, zeta-potential, and PDI were measured using dynamic light scattering (DLS) instrumentation (Zetasizer®Nano ZS90; Malvern Instruments, Malvern, UK). All reported results represent the mean of three independent test runs, with the DLS measurements maintained at a controlled temperature of 25 °C.

X-ray diffraction (XRD)

XRD analysis was performed to determine the crystalline structure of the bisabolol oxide A-loaded micellar/liposomal nanoparticles. The analysis was conducted using a Philips PW 1730 X-ray diffractometer (Netherlands) equipped with Cu Kα radiation (λ = 1.540598 Å). Data were collected at a current of 30 mA and a voltage of 30 kV, scanning diffraction angles (2θ) from 0° to 75° with a step size of 0.05°.

Anticancer activity assessments

Cell viability assay

The DU-145 human prostate cancer line and the HFF2 human fibroblast cell line were obtained from the National Cell Bank of Iran (NCBI, Pasteur Institute, Tehran, Iran), where routine authentication and quality control procedures are implemented. All cell lines were confirmed to be mycoplasma-free prior to experimentation. Cells were seeded in 96-well microplates and cultured in RPMI-1640 medium (Biowest, France) supplemented with 1% penicillin-streptomycin (Gibco, USA) and 10% fetal bovine serum (FBS). Cultures were maintained in a humidified atmosphere at 37 °C containing 5% CO_2. Cells were treated with varying concentrations (0, 20, 40, 80, and 100 µg/mL) of the bisabolol oxide A-loaded nanoparticles, free Paclitaxel, or empty PEG_{400}-OA (micellar/liposomal nanoparticles) for 24, 48 and 72 hours. The Bisabolol oxide A-loaded nanoparticles were dispersed in phosphate-buffered saline (PBS), which was also used in the control wells to ensure identical solvent conditions. The final volume in each well was adjusted to 100 µL.

Cell viability was determined using the MTT assay according to the manufacturer's protocol. At the specified time points, MTT dye (0.5 mg/mL, Sigma-Aldrich, USA) was added to treated and untreated cells and incubated for 3 hours at 37 °C. Following incubation, the resulting formazan crystals were dissolved by adding dimethyl sulfoxide (DMSO), followed by a 15 minutes incubation. The optical density (OD) was measured at 570 nm with a reference wavelength of 630 nm using a microplate reader (ELx800, BioTek, Winooski, VT, USA). Cell viability was calculated as the percentage of viable treated cells relative to untreated control cells. All experiments were performed in triplicate, and results were compared to the respective controls [45]. The cytotoxicity was quantified using the following formula:

$$Cytotoxicity\,(\%) = \frac{OD_{(Test)}}{OD_{(Control)}} \times 100$$

Apoptosis measurement via Annexin V-FITC/PI staining

The induction of apoptosis was evaluated in DU-145 cells exposed to a specific concentration (55.44 µg/mL) of the bisabolol oxide A-loaded nanoparticles. To determine apoptosis levels, 1×10^6 cells were seeded into two T25 flasks and allowed to adhere for 24 hours. The cells were then treated with either 0 µg/mL (control) or 55.44 µg/mL of the bisabolol oxide A-loaded nanoparticles for an additional 24 hours. Apoptosis levels were determined by dual staining with Annexin V-FITC and propidium iodide (PI) according to the manufacturer's protocol. Following staining, the samples were analyzed using flow cytometry (BD FACSCalibur, BD Biosciences, San Jose, CA) [46].

Table 1 Sequence of miRNA primers used for qRT-PCR

Primer name	Primer sequence
miR-181a-F	5′-ACCAACATTCAACGCTG-3′
miR-34a-F	5′-AGGGTGGCAGTGTCTTAG-3′
SNORD47	5′-ATCACTGTAAAACCGTTC-3′
miR universal-R	5′-GAGCAGGGTCCGAGGT-3′

Wound healing (scratch) assay

The wound healing scratch assay was employed to assess two-dimensional cell migration following treatment with bisabolol oxide A loaded nanoparticles [47]. DU-145 cells (50×10^3 cells/well) were seeded in a six-well plate and allowed to adhere for 24 hours. A uniform scratch was created across the cell monolayer using the sterilized tip of a 100 µL pipette. After washing with PBS to remove cellular debris, the cells were treated with 0 µg/mL (control) or 55.44 µg/mL of the bisabolol oxide A-loaded nanoparticles for 24 hours. Images of the wound gap were captured using an inverted microscope (Nikon, USA) at 0 and 24 hours to quantify the extent of wound closure.

Quantitative assessment of miR-181a and miR-34a expression levels

The expression levels of miR-181a and miR-34a were quantitatively assessed using qRT-PCR. Total RNA was extracted from DU-145 cells treated (with bisabolol oxide A-loaded nanoparticles for 24 hours) and untreated cells using the RNX-Plus kit (SinaClon, Tehran, Iran). Complementary DNA (cDNA) synthesis was performed using the BON Stem High-Sensitivity microRNA 1st-Strand cDNA Synthesis Kit (Stem Cell Technology Research Center, Tehran, Iran). For cDNA synthesis, total RNA and BON-RT adaptor (stem-loop primers, 1 µM) were incubated at 75 °C for 5 minutes in a thermocycler (Bio-Rad, USA). Subsequently, dNTPs, RT enzyme, and reaction buffer were added. The reaction cycling involved incubation at 37 °C for 10 minutes, followed by 55 °C for 60 minutes, and a final denaturation step at 70 °C for 10 minutes. qRT-PCR was conducted using the Universal SYBR qPCR Master Mix (2x) (Stem Cell Technology Research Center, Tehran, Iran) on a StepOne Real-Time PCR System (Applied Biosystems, USA). The qRT-PCR amplification program comprised an initial denaturation step at 95 °C for 5 minutes, followed by 40 cycles at 95 °C for 5 seconds and 60 °C for 5 seconds. The specific primers utilized for this analysis are listed in Table 1, with SNORD47 serving as the endogenous reference control. The relative expression levels of the miRNAs were evaluated using the $2^{-\Delta\Delta Ct}$ method.

In silico prediction of miR-181 and miR-34a potential targets

The putative target genes regulated by miR-181a and miR-34a implicated in apoptosis, cell adhesion, and migration pathways were identified via computational analysis using established predictive algorithms. Specifically, miRWalk (http://mirwalk.umm.uni-heidelberg.de/) and TargetScan (https://www.targetscan.org/vert_80/) were utilized. These algorithms incorporate critical parameters, including the degree of complimentary between the miRNAs seed sequence and the 3´- untranslated region (3′-UTR) of potential target mRNAs and the thermodynamic stability of the resulting miRNA-mRNA heteroduplex, thereby ensuring robust prediction of functionally relevant targets.

Expression pattern analysis of predicted target genes

The transcription levels of predicted downstream targets of miR-181a and miR-34a, specifically TP53 (encoding *P53*), *CASP9* (caspase 9), *CTNNB1* (β-catenin), *EGFR* (Epidermal Growth Factor Receptor), and *SMAD3* (SMAD family member 3)—were subsequently analyzed by qRT-PCR. After 24 hours of treatment with bisabolol oxide A-loaded nanoparticles, total RNA was extracted from both treated and untreated DU-145 cells using the Total RNA Extraction Mini-Kit (Yekta Tajhiz Azma, Iran), following the manufacturer's guidelines. Subsequently, complementary DNA (cDNA) synthesis was completed using the appropriate cDNA synthesis kit (Yekta Tajhiz Azma, Iran). The qRT-PCR protocol involved an initial denaturation step at 95 °C for 3 minutes, followed by 40 amplification cycles comprising denaturation at 95 °C for 5 seconds, annealing at 60 °C for 5 seconds, and extension at 75 °C for 10 seconds. Reactions were carried out using the SYBR Green qPCR Mix (Yekta Tajhiz Azma, Iran), on a Rotor-Gene Q instrument (QIAGEN, Germany), employing SYBR Green fluorescence for detection. The expression levels of the target genes were quantified in triplicate and normalized against the housekeeping gene, glyceraldehyde-3-phosphate dehydrogenase (*GAPDH*) using the $2^{-\Delta\Delta Ct}$ equation. Both forward and reverse primer sequences, which were validated via Primer-BLAST (https://blast.ncbi.nlm.nih.gov/Blast.cgi) and are listed in Table 2, demonstrated an amplification efficiency greater than 99%.

Table 2 Sequence of primers used for qRT-PCR

Primer name	Primer sequence	Length of production	Reference
P53-F	5`- CCTGAGGTTGGCTCTGAC –3`	259 bp	This study
P53-R	5`- GCAGTGCTCGCTTAGTGC –3`		
Casp9-F	5′-CCTGCTTAGGGTCGCTAATG-3′	257 bp	This study
Casp9-R	5′-GCTAAGAGCCTGTCTGTCAC-3′		
SMAD3-F	5′-AGAGACACCAGTTCTACCTCC-3′	222 bp	This study
SMAD3-R	5′-GAACCTGCGTCCATGCTG-3′		
EGFR-F	5′-AGACCATCCAGGAGGTGG-3′	393bp	This study
EGFR-R	5′-TCAGTTTCTGGCAGTTCTCC-3′		
CTNNB-F	5′-GACAATGGCTACTCAAGCTG-3′	264 bp	This study
CTNNB-R	5′-GCATACTGTCCATCAATAT-CAGC-3′		
GAPDH-F	5′-CTCAAGATCATCAGCAAT-GCCTCC-3′	113 bp	This study
GAPDH-R	5′-ATGGCATGGACTGTGGTCAT-GAG-3′		

Western blot analysis

Total proteins extracts were prepared from DU-145 cells (1×10^6) treated with bisabolol oxide A-loaded micellar/liposomal nanoparticles and from untreated control cells. Lysis buffer comprised a general cocktail supplemented with EDTA, Sodium Deoxycholate, SDS, protease inhibitors, and 1% Triton X-100. Protein concentrations were subsequently quantified using the Bradford protein assay. Equal amounts of proteins from both groups were separated on 10% SDS-PAGE. The separated proteins were electroblotted onto polyvinylidene fluoride (PVDF) membranes (Bio-Rad, USA). The membranes were blocked using a 5% skim milk, and incubated overnight at 4 °C with primary antibodies against B-Catenin (92 kDa), EGFR (80 kDa), and GAPDH (37 kDa, Santa Cruz Biotechnology, USA). After washing with TBS-T buffer, the membranes were incubated with HRP-conjugated secondary antibodies (Santa Cruz Biotechnology, USA) for 75 minutes at room temperature. The protein bands were visualized using ECL reagent and quantified using ImageJ software.

Molecular docking analysis

Docking study

Molecular docking is a widely used computational technique to investigate the chemical interaction landscape between ligands and protein receptors [48, 49]. The three-dimensional structures of β-catenin (PDB ID: 1JDH) and EGFR (PDB ID: 4WKQ) were retrieved from the Protein Data Bank, while the chemical structures of bisabolol oxide A, bisabolol oxide B and 5,8,11-heptadecatriynoic acid methyl ester (Fig. 1a) were sourced from the PubChem database. Prior to molecular docking simulations, co-crystallized ligands and water molecules were removed from the protein structures. Polar hydrogens were added, and partial atomic charges were assigned using the Gasteiger and Marsili method [50].

Protein structures were energy-minimized using Chimera software, employing 1000 steps of the steepest descent algorithm followed by 10 steps of the conjugate gradient algorithm [51]. Ligand structures were optimized using OpenBabel with the Universal Force Field (UFF) and the conjugate gradient algorithm [52]. The optimized ligands and the target protein structure (PDB format) were imported into PyRx 0.8 and converted to

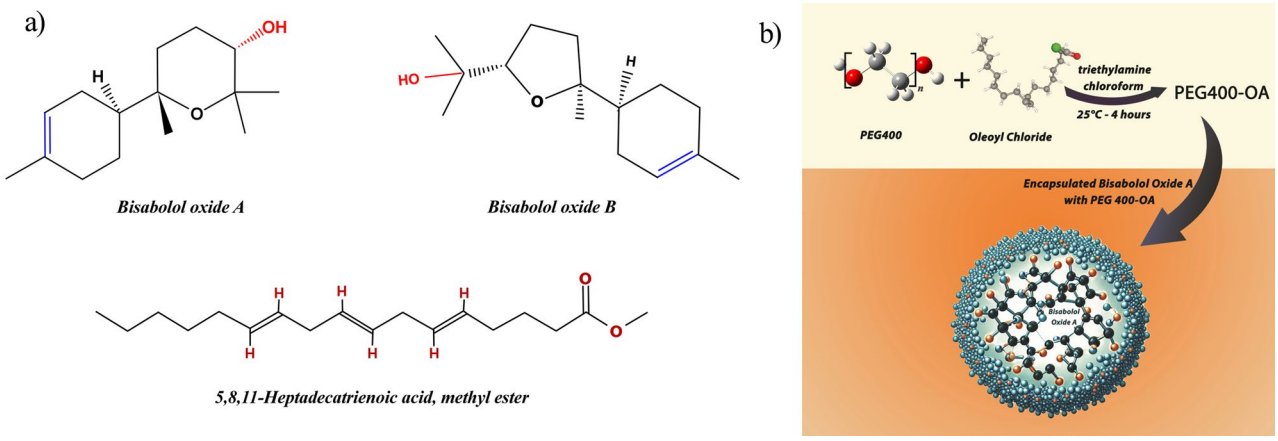

Fig. 1 Molecular structure and synthesis pathway. **a**) Structures of the three primary chamomile components utilized for molecular docking studies, **b**) schematic representation of the synthesis of PEG400-OA nanoparticles and the subsequent encapsulation of bisabolol oxide a to yield bisabolol oxide A-loaded micellar/liposomal nanoparticles

PDBQT format. Following the definition of the grid box surrounding the protein's active site (Supplementary Table 1), molecular docking simulations were conducted using the AutoDock Vina plugin [53] integrated into the PyRx platform [54]. The chemical interaction landscape between the ligands and receptors was visualized and analyzed using Discovery Studio Visualizer software. Furthermore, to validate the docking parameters, the co-crystallized ligand was redocked and the resulting root mean square deviation (RMSD) values were calculated [55].

Drug-like and pharmacokinetics properties assessment

The chemical compounds were evaluated for drug-like properties and pharmacokinetics using the SwissADME web tool [56]. This assessment included parameters such as topological polar surface area (TPSA), solubility (Log S), and gastrointestinal (GI) absorption [57]. Additionally, the ProTox-II webserver was utilized to analyze the hepatotoxicity of the compounds and other toxicity endpoints, including carcinogenicity, immunotoxicity, mutagenicity, and cytotoxicity.

Statistical analysis

All quantitative experimental data are reported as the mean ± standard deviation (SD). Each cellular experiment was performed independently in triplicate, and gene expression analyses (qRT-PCR) were conducted in a minimum of two independent biological replicates. Before inferential testing, the normality of qRT-PCR data distributions was rigorously assessed using the Shapiro-Wilk test. For multi-group comparisons in the MTT assays, a one-way analysis of variance (ANOVA) was applied. Conversely, unpaired Student's t-tests were utilized for all two-group comparisons in microRNA and target gene expression analyses. Statistical significance was conventionally defined as $p < 0.05$. All statistical computations were executed using GraphPad Prism software, version 9.4.1 (GraphPad Software Inc., La Jolla, CA, USA).

Results

Physicochemical characterization of bisabolol oxide A-Loaded nanoparticles

Bisabolol oxide A, an important active component derived from *Matricaria chamomilla* (Fig. 1a), was successfully encapsulated into PEG_{400}-OA nanoparticles to produce Bisabolol oxide A-loaded micellar/liposomal nanoparticles. A schematic representation of the PEG400-OA synthesis and the subsequent Bisabolol oxide A encapsulation is depicted in Fig. 1b.

Fourier-Transform Infrared Spectroscopy (FT-IR) analysis was performed to confirm the successful incorporation of Bisabolol oxide A into the nanocarrier matrix (Fig. 2). The FT-IR spectra for Bisabolol oxide A, the bare nanoparticles, and the Bisabolol oxide A-loaded nanoparticles exhibited key overlapping spectral features. A broad absorption band observed between 3200 and 3450 cm^{-1} was attributed to the O-H stretching vibrations, present in both the alcoholic groups of bisabolol oxide A and hydroxyl groups of the PEG chains in the nanoparticles.

A prominent peak at 1650 cm^{-1}, indicative of C = C stretching vibrations from olefinic groups, was consistent with the chemical structure of bisabolol oxide A (Fig. 2). Furthermore, the characteristic C-O stretching vibrations associated with etheric and alcohol groups were confirmed by a band in the 1100–1250 cm^{-1} region. Crucially, the presence of an absorption peak near 1735 cm^{-1}, corresponding to the C = O stretching vibrations of the ester group within bisabolol oxide A, provides definitive spectral evidence of bisabolol oxide A's successful loading

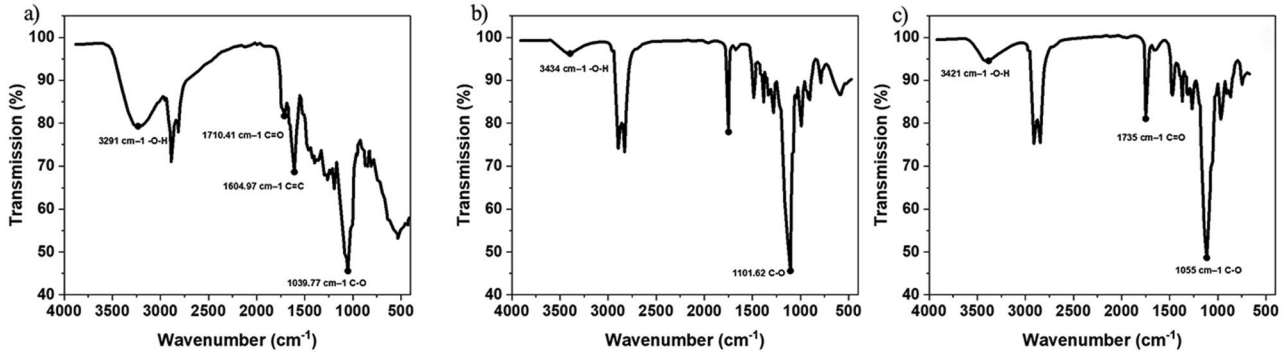

Fig. 2 Fourier-Transform Infrared (FT-IR) spectra. Comparison of the FT-IR spectra for **a**) pure bisabolol oxide A, **b**) PEG_{400}-OA and c) the resultant bisabolol oxide A-loaded micellar/liposomal nanoparticles. This spectral analysis confirms the successful incorporation and encapsulation of bisabolol oxide a within nanocarrier system

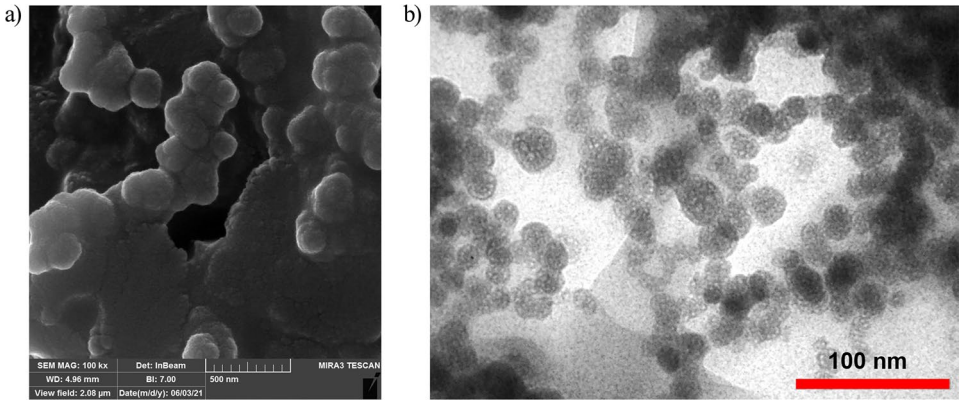

Fig. 3 Morphology and size characterization of bisabolol oxide A-loaded nanoparticles. **a**) Scanning electron micrograph (SEM) illustrating particle sizes in the range of 46–59 nm. **b**) Transmission electron micrograph (TEM) confirming the spherical morphology and monodisperse nature of the nanoparticles, with measured sizes between 35 and 50 nm

and chemical association within the nanoparticle structure (Fig. 2). These spectral findings collectively confirm the successful loading of bisabolol oxide A within the micellar/liposomal nanoparticles.

Scanning electron microscopy (SEM) analysis revealed nanoparticle sizes ranging from 46 to 59 nm. This micrograph (Fig. 3a) illustrates a uniform size distribution, characterized by a visually consistent, symmetrical, and orderly arrangement. To further elucidate the morphology and confirm size parameters, transmission electron microscopy (TEM) was performed. The TEM analysis confirmed the formation of spherical, monodisperse polymeric nanoparticles. Images acquired at multiple magnifications revealed a size distribution of 35–50 nm (Fig. 3b). These collective findings confirm the uniformity and nanoscale dimensions of the bisabolol oxide A-loaded nanoparticles.

The thermal stability of the synthesized bisabolol oxide A-loaded nanoparticles was investigated using Thermogravimetric Analysis-Differential Thermogravimetric Analysis (TGA-DTG). The TGA-DTG curve exhibited an initial mass loss of approximately 4% occurring at 66.67 °C, attributed to the evaporation of surface hydroxyl groups. Crucially, no significant degradation of organic components was observed up to 200 °C, as indicated by the absence of mass loss in this range (Fig. 4a). A subsequent mass change recorded at 380 °C corresponds to the decomposition of the incorporated organic functional groups. These data confirm that the bisabolol oxide A-loaded nanoparticles possess excellent thermal stability up to 200 °C, suggesting stability for applications sensitive to moderate thermal stress. Furthermore, the physicochemical stability of bisabolol oxide A-loaded micellar/liposomal nanoparticles was evaluated using DLS and zeta potential measurements. Based on DLS analysis, the hydrodynamic sizes of the nanoparticles after one week (Fig. 4b) and one year (Fig. 4c) were 80 nm and 133.9 nm, respectively. The slight increase in particle size after one year indicates excellent long-term stability. Additionally, the zeta potential values of the nanoparticles were measured as −40.1 mV after one week (Fig. 4d) and −24.8 mV after one year (Fig. 4e). Although a mild reduction in zeta potential was observed over time, the

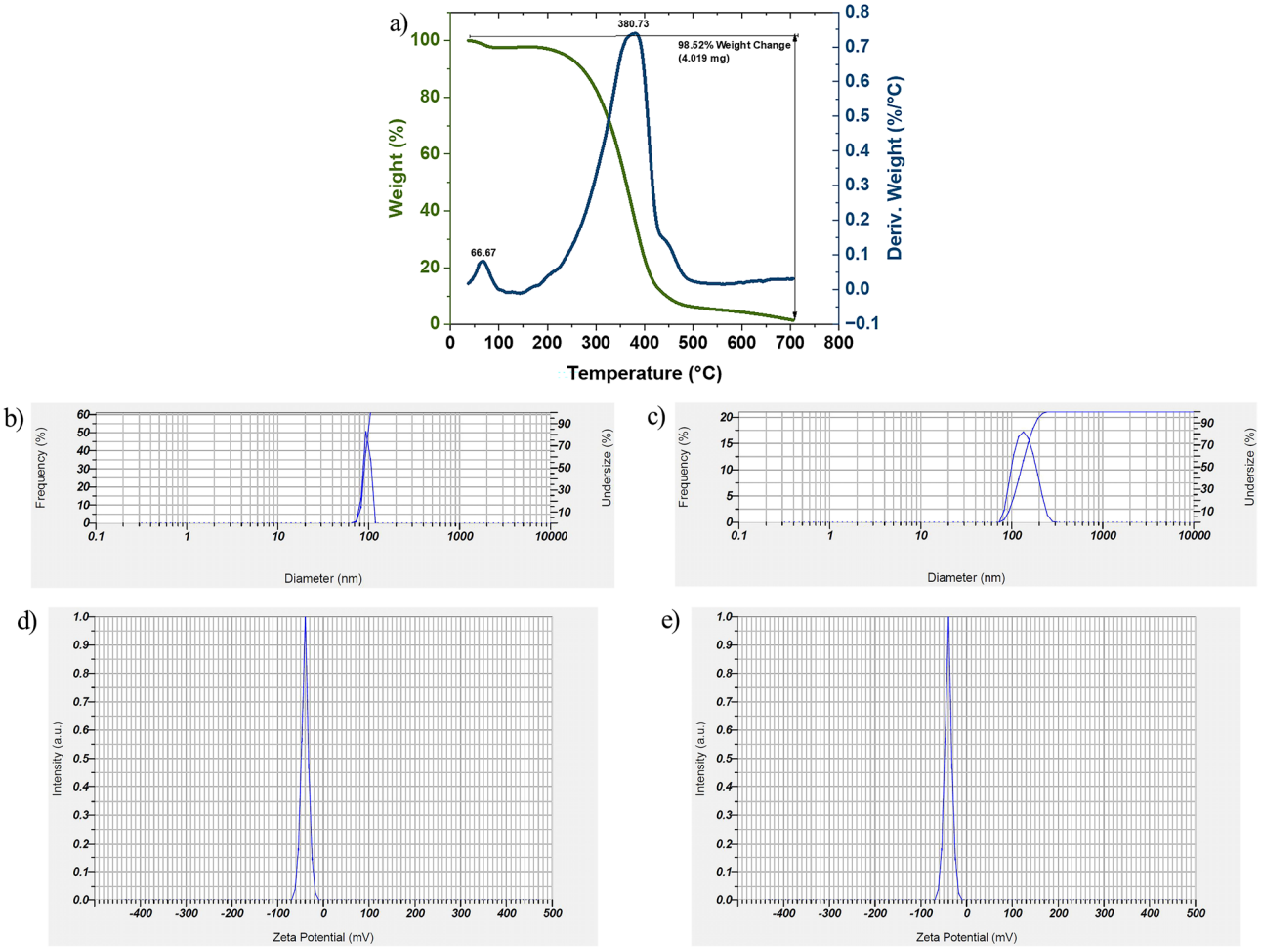

Fig. 4 Thermal and physicochemical stability of bisabolol oxide A-loaded micellar/liposomal nanoparticles. **a**) TGA-DTG profile demonstrating the thermal stability of the nanoparticles up to approximately 380 °C. **b**,**c**) DLS size distribution of nanoparticles after one week and one year, showing mean diameters of 80 nm and 133.9 nm, respectively, indicating good stability. **d**,**e**) zeta potential values of nanoparticles after one week (–40.1 mV) and one year (–24.8 mV), demonstrating a stable colloidal dispersion over time

high negative surface charge confirms the good colloidal stability of the nanoparticles even after one year.

The XRD pattern of the micellar/liposomal nanoparticles (Fig. 5a) exhibited a broad diffraction band in the range of 2θ = 20°–29°, which is associated with PEG_{400}, along with sharp peaks at 31°, 45°, and 57° corresponding to oleic acid. Similarly, the XRD spectrum of the bisabolol oxide A-loaded micellar/liposomal nanoparticles (Fig. 5b) showed the same peaks with only minor changes, which are characteristic of liposomal nanocarriers. The absence of the characteristic peaks of bisabolol oxide A confirms its successful encapsulation within the micellar/liposomal nanoparticles.

Anticancer evaluations

Antiproliferative activity of bisabolol oxide A-Loaded micellar/liposomal nanoparticles

The MTT assay demonstrated that treatment with bisabolol oxide A-loaded micellar/liposomal nanoparticles induced a dose- and time-dependent reduction in DU-145 cell proliferation. The calculated IC_{50} values were 55.44 µg/mL, 46.21 µg/mL, and 43.59 µg/mL at 24, 48, and 72 hours, respectively (Fig. 6a). The IC_{50} values of Paclitaxel (as a positive control) were > 100 µg/mL, 86.77 µg/mL, and 62.37 µg/mL at 24, 48, and 72 hours, respectively (Fig. 6b). Conversely, HFF2 normal cells exhibited high viability, remaining 80% when exposed to bisabolol oxide A-loaded micellar/liposomal nanoparticles at concentrations ranging from 0 to 100 µg/mL for both 24 and 48 hours. Even after 72 hours, viability remained ~60% at concentrations below 80 µg/mL (Fig. 6c). Meanwhile, empty PEG_{400}-OA nanoparticles (vehicle control) demonstrated more than 80% cell viability in both HFF-2 normal cells (Fig. 5d) and DU-145 prostate cancer cells (Fig. 6e).

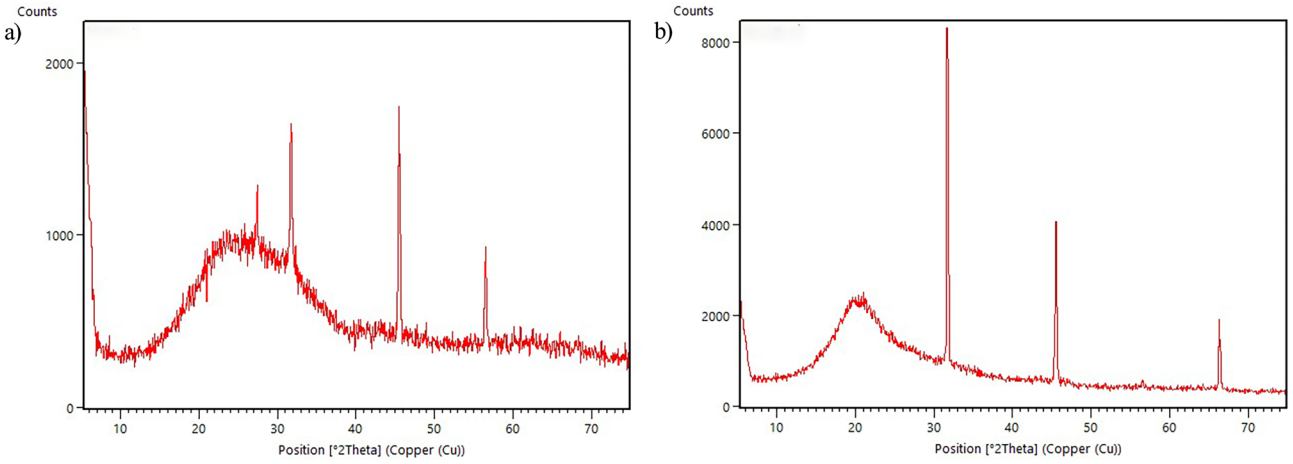

Fig. 5 X-ray diffraction (XRD) patterns of **a**) empty micellar/liposomal nanoparticles and **b**) bisabolol oxide A-loaded micellar/liposomal nanoparticles

Apoptosis analysis following treatment with bisabolol oxide A-Loaded micellar/liposomal nanoparticles

Annexin V-FITC/PI analysis revealed that bisabolol oxide A-loaded micellar/liposomal nanoparticles (IC_{50} = 55.44 µg/mL) significantly induced apoptosis in DU-145 prostate cancer cells after 24 hours. Specifically, the population of cells in early apoptosis (Annexin V^+/PI) increased from 3.41% in untreated controls to 31.6% in treated cells. Late apoptosis (Annexin V^+/PI^+) also rose significantly, increasing from 4.66% to 18.1% in treated cells. Necrosis was observed in 9.11% of treated cells, compared to 2.75% in the untreated group (Fig.s 7a-b). The percentage of late apoptosis increased at higher dose (85.44 µg/mL) relative to the IC_{50} (55.44 µg/mL), while the percentage of early apoptosis decreased at higher dose, attributed to the further disruptive effect of the higher agent dose on DU-145 cancer cells (Fig. 7c). Furthermore, the total percentage of apoptotic cells quantified across three concentrations (0, IC_{50} = 55.44, and 85.44 µg/mL) increased dose-dependently, recorded as 8.63 ± 0.79%, 50.7 ± 1.84%, and 77.2 ± 3.39%, respectively (Fig. 7d).

Inhibition of cell migration by bisabolol oxide A-Loaded nanoparticles

The anti-migratory effects of bisabolol oxide A-loaded micellar/liposomal nanoparticles on DU-145 cells were evaluated using a scratch assay. Following the scratch procedure, cells were treated or left untreated with the nanoparticles (IC_{50} = 55.44 µg/mL) for a 24-hour incubation period. The results clearly demonstrated that treatment with the encapsulated bisabolol oxide A significantly inhibited cell migration compared to the untreated control group over the 24-hour duration (Fig. 8).

Deregulation of miR-181a and miR-34a expression following bisabolol oxide a treatment

The expression profiles of miR-181a and miR-34a were quantified in DU-145 prostate cancer cells following treatment with bisabolol oxide A-loaded nanoparticles (IC_{50} = 55.44 µg/mL). Quantitative RT-PCR analysis demonstrated a significant upregulation of the tumor-suppressive miR-34a, exhibiting a 2.31 ± 0.16-fold increase in treated cells relative to the untreated control group (Fig. 9a). In contrast, the oncogenic microRNA, miR-181a, was significantly downregulated, showing a 1.72 ± 0.03-fold reduction (Fig. 9c).

Gene expression profiles modulated by bisabolol oxide A

In silico analysis predicted that miR-181a and miR-34a target genes are functionally involved in cell migration and apoptosis pathways (Table 3). Treatment of DU-145 cells with bisabolol oxide A-loaded nanoparticles (IC_{50} = 55.44 µg/ml) induced significant alterations in target gene expression compared to the untreated control. Quantitative RT-PCR confirmed the downregulation of several miR-34a targets implicated in cell adhesion, specifically *β-catenin* (*CTNNB*), *SMAD3*, and *EGFR* (Fig. 9b). Conversely, treatment upregulated pro-apoptotic genes, *P53* and *CASP9*, which are predicted targets of miR-181a. These collective transcriptomic changes underscore the compound's mechanism in inducing apoptosis in DU-145 cells (Fig. 9d).

As illustrated by the proposed mechanistic model (Fig. 10), encapsulation of bisabolol oxide A into micellar/liposomal nanoparticles (IC_{50} = 55.44 µg/mL) leads to the upregulation of the tumor-suppressive miR-34a and the subsequent downregulation of its target genes involved in cell migration and invasion. This reduction in the expression of key miR-34a targets, specifically EGFR and β-catenin, in treated DU-145 cells was validated through western blot analysis (Fig. 11) and functional assessment

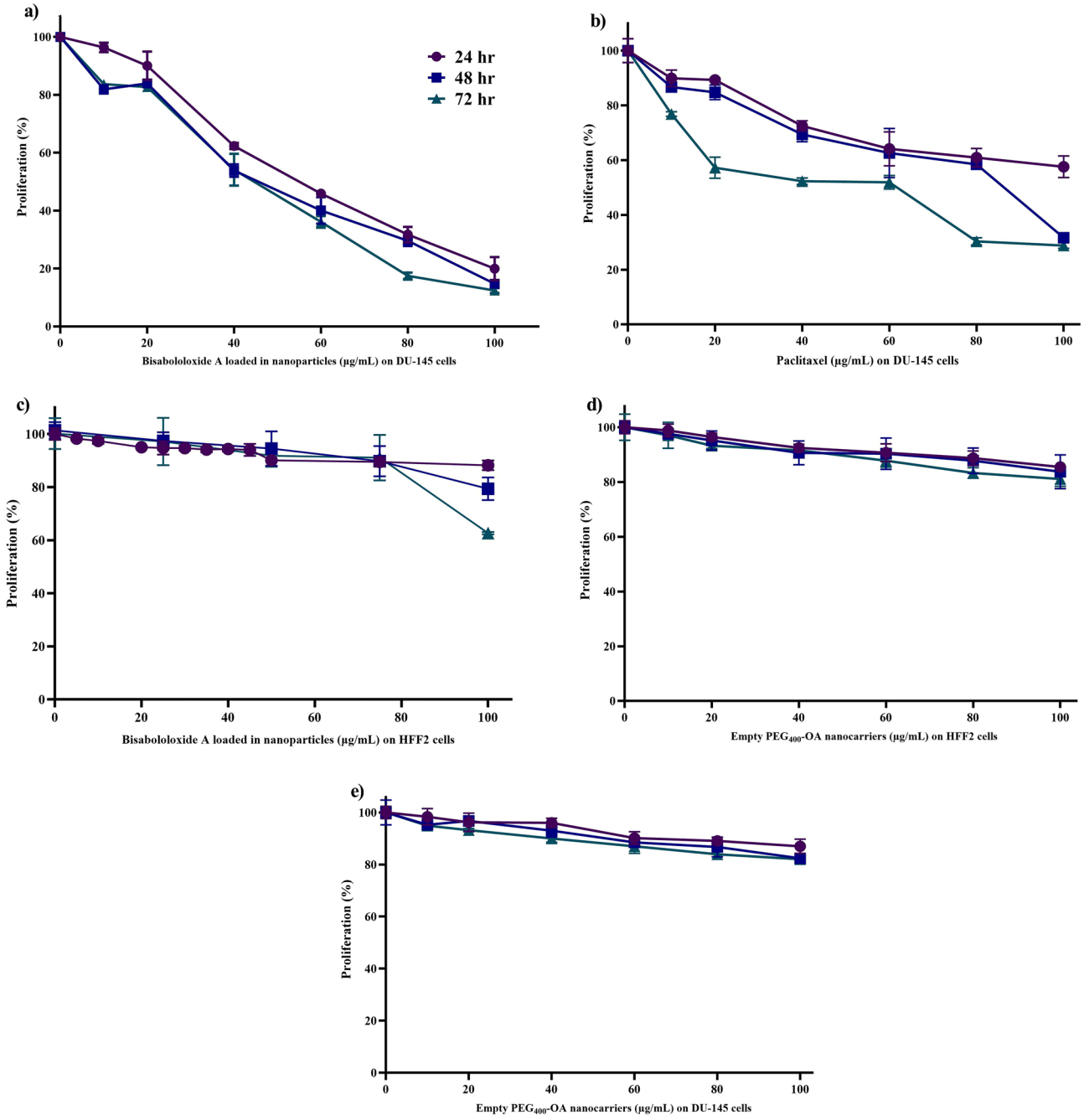

Fig. 6 Comparative antiproliferative activity assessed by MTT assay. **a**) Viability of DU-145 prostate cancer cells following treatment with bisabolol oxide A-loaded micellar/liposomal nanoparticles and **b**) Paclitaxel (positive control). Cytotoxicity of **c**) Bisabolol oxide A-loaded micellar/liposomal nanoparticles and **d**) Empty PEG_{400}-OA nanocarriers on HFF2 normal human fibroblast cells, and **e**) On DU-145 prostate cancer cells. The inhibitory effects of various treatments including bisabolol oxide A-loaded micellar/liposomal nanoparticles, empty PEG_{400}-OA nanoparticles (vehicle control), and the chemotherapeutic agent paclitaxel, were assessed at doses of 0, 20, 40, 80, and 100 µg/ml after 24, 48 and 72 hours. Data are expressed as mean ± SD. Statistical significance relative to untreated controls is indicated by asterisks (***$p < 0.001$)

via the wound healing assay. Furthermore, the schematic model (Fig. 10) suggests that the nanoparticles also mediate the downregulation of the oncomiR miR-181a, resulting in the upregulation of its pro-apoptotic target genes, a mechanism functionally confirmed by Annexin V-FITC/PI staining results.

Molecular docking analysis

Docking simulations (β-catenin)

The best binding affinities observed for β-catenin-bisabolol oxide A, β-catenin-bisabolol oxide B, and β-catenin-5,8,11-heptadecatriynoic acid methyl ester

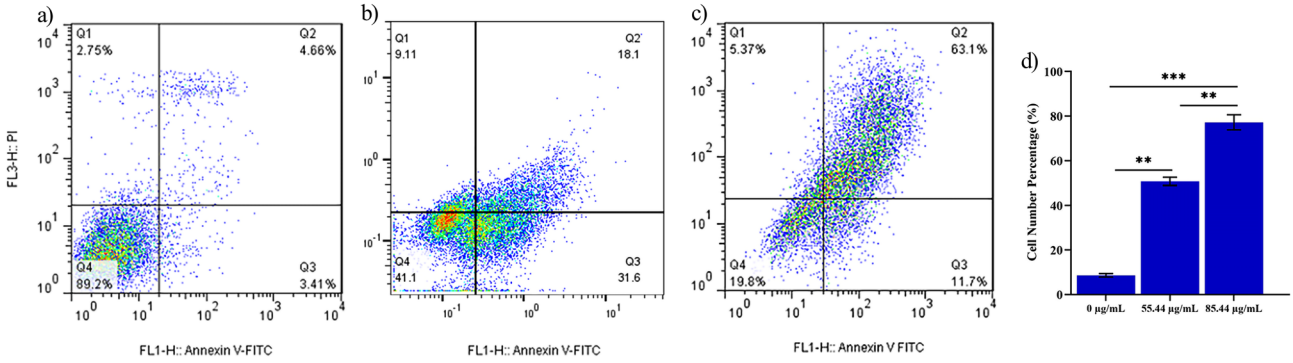

Fig. 7 Apoptosis induction in DU-145 cells determined by Annexin V-FITC/PI flow cytometry. Representative flow cytometry plots showing staining patterns for **a**) untreated control cells, cells treated with bisabololoxide A-loaded micellar/liposomal nanoparticles at **b**) the IC50 concentration (55.44 µg/mL) and **c**) a higher concentration (85.44 µg/mL). **d**) Quantitative representation of the total apoptotic cell percentage across varying nanoparticle concentrations. Quadrants are defined as Q1 (necrosis), Q2 (late apoptosis), Q3 (early apoptosis), and Q4 (viable cells). Data from duplicate experiments are presented as mean±SD. Statistical significance relative to the untreated control is indicated (**$p < 0.01$, and ***$p < 0.001$)

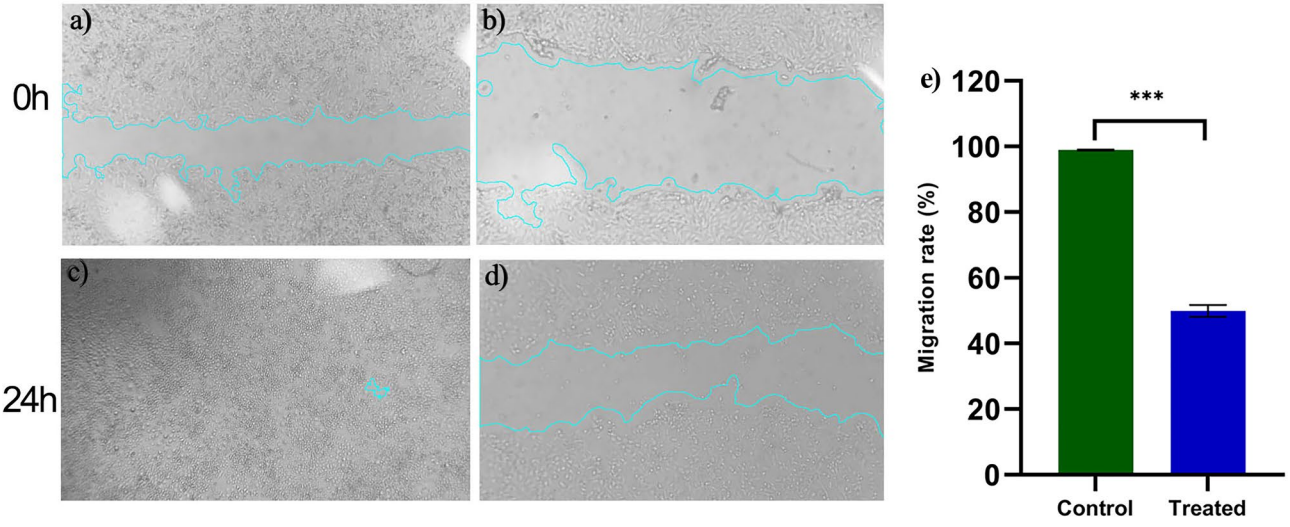

Fig. 8 Inhibition of DU-145 cell migration via wound healing (scratch) assay. Representative images illustrating wound closure over 24 hours: (**a, c**) Untreated control cells at 0 hour and 24 hours, respectively. (**b, d**) Cells treated with bisabolol oxide A-loaded micellar/liposomal nanoparticles (IC_{50} = 55.44 µg/mL) after b) 0 hour and **d**) and 24 hours, respectively. Quantification of the migration inhibition demonstrates that the encapsulated bisabolol oxide A-significantly reduced cancer cell motility after 24 hours

complexes were, respectively, −6 kcal/mol, −5.7 kcal/mol, and −4.8 kcal/mol (Table 4).

The β-catenin-bisabolol oxide A complex manifests two hydrogen bonds with Trp338 and Arg376 (Fig. 12a). β-catenin engages in interactions with both bisabolol oxide B and 5,8,11-heptadecatriynoic acid methyl ester through three H-bonds. Bisabolol oxide B involves Arg469, Ser473, and Asn516 (Fig. 12b), while 5,8,11-heptadecatriynoic acid methyl ester interacts through Trp338, Arg342, and Asn380 (Fig. 12c). Concerning hydrophobic interactions, bisabolol oxide A exhibits seven interactions (alkyl and pi-alkyl) involving residues Tyr306, Arg342, Lys345, Val346, Arg376, and Trp383 (Fig. 12a), while 5,8,11-heptadecatriynoic acid methyl ester forms nine alkyl and pi-alkyl interactions through Tyr306, Trp338, Arg342, Lys345, Val349, and Trp383 (Fig. 12c). For bisabolol oxide B, only four alkyl interactions with residues Arg469, Lys508, and Val511 was observed (Fig. 12b).

Docking simulations (EGFR)

The computed best binding affinities for the EGFR-bisabolol oxide A, EGFR-bisabolol oxide B, and EGFR-5,8,11-heptadecatriynoic acid methyl ester complexes were, respectively, −5.9 kcal/mol, −6.6 kcal/mol, and −5.2 kcal/mol (Table 4). Both bisabolol oxide A and bisabolol oxide B interact with EGFR through one hydrogen bond (Figs. 13a, 13b), whereas 5,8,11-heptadecatriynoic acid methyl ester forms five H-bonds with EGFR via residues Leu798, Leu799, Asp800, and Arg841 (Fig. 13c).

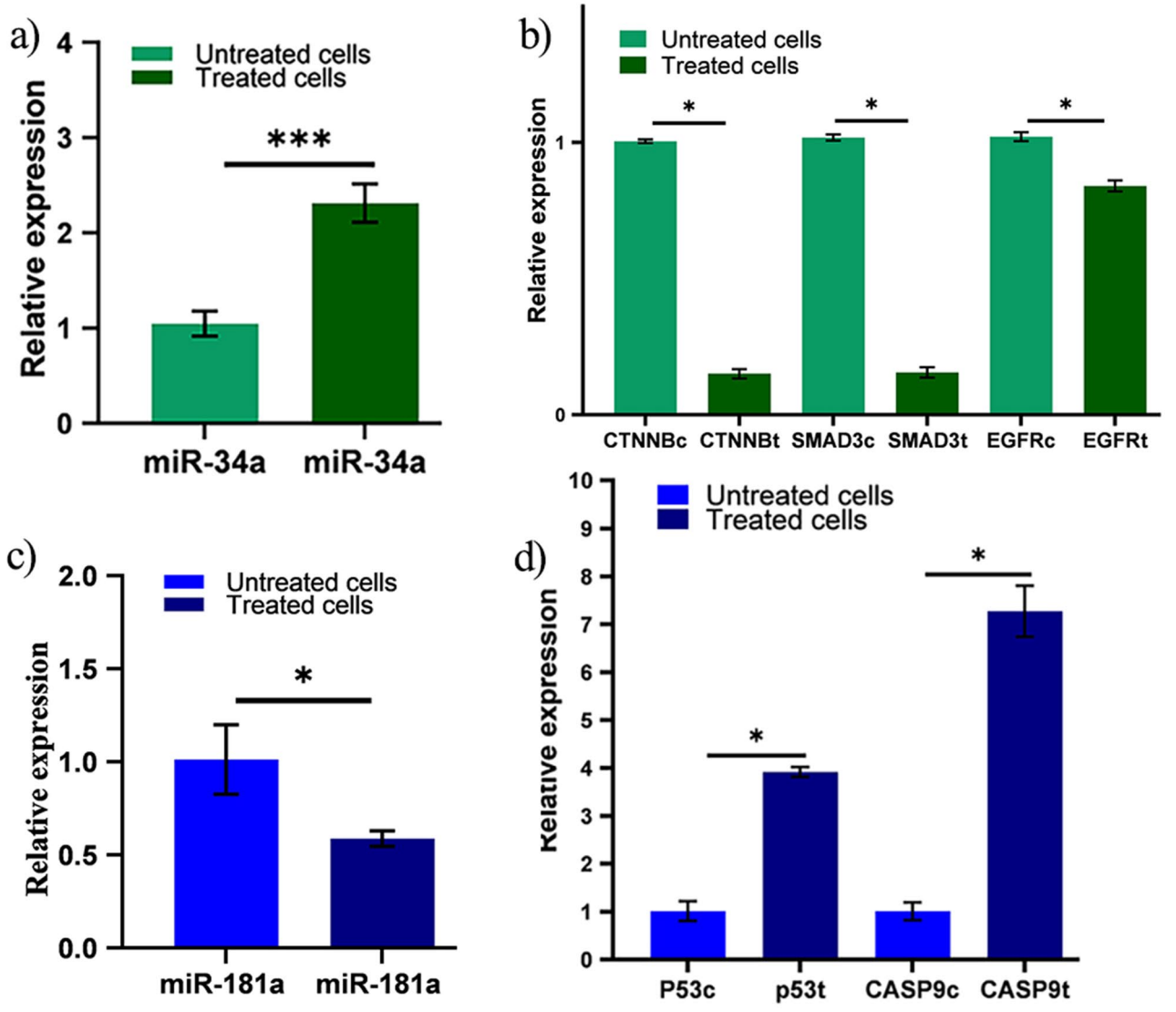

Fig. 9 Quantitative RT-PCR analysis of target gene and miRNA expression. Comparison of DU-145 cells treated (t) with bisabolol oxide A-loaded nanoparticles (IC50 = 55.44 µg/mL) versus untreated controls (c). **a**) Relative expression of miR-34a (upregulated). **b**) Expression levels of predicted miR-34a targets involved in cell migration pathways *β-catenin* (*CTNNB*), *SMAD3* and *EGFR* (downregulated) **c**) Relative expression of miR-181a (downregulated). **d**) Expression levels of predicted miR-181a targets involved in apoptosis pathways (*P53,* and *CASP9*) (upregulated). Data from triplicate experiments are shown as mean ± SD. Statistical significance is indicated by asterisks (*$p < 0.05$, and ***$p < 0.001$)

Both the EGFR-bisabolol oxide B and EGFR-5,8,11-heptadecatriynoic acid methyl ester complexes display nine hydrophobic alkyl interactions (Fig.s 13b-c), while the EGFR-bisabolol oxide A complex exhibits ten alkyl interactions (Fig. 13a). Residues Leu718, Val726, and Leu844 are common amino acids among the three EGFR-ligand complexes, contributing to the hydrophobic interactions (Fig. 13). Table 4 lists other residues involved in hydrophobic networks regulated by EGFR and chemical compounds.

Validation of the docking procedure was achieved by redocking the co-crystallized gefitinib into the EGFR active site. The superimposed structures of the redocked and crystallographic ligands showed a low RMSD value of 1.63 Å, confirming the accuracy of the docking protocol (Fig. 14).

Drug-likeness and pharmacokinetics properties

For the assessment of drug-likeness in the active compounds, the SwissADME web tool was utilized. The Lipinski's rule of five criteria, encompassing molecular weight (<500 Da), hydrogen bond donors (<5), hydrogen bond acceptors (<10), and LogP (<5), indicated that all compounds exhibit drug-like features (Table 5). Additionally, bioavailability radars were generated for these

Table 3 Some potential targets of miRnas related to cell migration and apoptosis pathways

miRNA	Potential target	Gene name
miR-34a	In the cell migration and invasion pathway	
	CTNNB1	Catenin beta 1
	CTNND1	Catenin delta 1
	CTNND2	Catenin delta 2
	EGFR	Epidermal Growth Factor Receptor
	SMAD3	SMAD family member3
	MMP2	Matrix Metallopeptidase 2
	MMP14	Matrix Metallopeptidase 14
miR-181a	In apoptotic pathways	
	APAF1	Apoptotic Peptidase Activating Factor 1
	BAX	BCL2 associated X
	CASP2	Caspase 2
	CASP6	Caspase 6
	CASP8	Caspase 8
	CASP9	Caspase 9
	CASP10	Caspase 10
	CDH1	E-cadherin
	ITGB8	Integrin beta 8
	CNTN4	Contactin 4
	PCDHA1	protocadherin alpha 1
	PCDHA2	protocadherin alpha 2

compounds, confirming their compliance with drug-likeness criteria (Fig. 15).

Pharmacokinetics properties were assessed using the SwissADME web tool. The topological polar surface area (TPSA) of all compounds was less than 30 $Å^2$, signifying high absorption and favorable permeability (Table 6). The LogS prediction ranging from −2.76 to −4.17 confirms their substantial solubility. High value in gastrointestinal (GI) absorption further denotes their potential suitability for oral administration. Moreover, none of the three compounds were identified as P-glycoprotein substrates, indicating resistance to elimination by P-glycoprotein (Table 6, Fig. 15).

According to the predictive analysis on the inhibition potential against CYP450 isoforms (CYP1A2, CYP2C19, CYP2C9, CYP2D6, CYP3A4), bisabolol oxide A and bisabolol oxide B showed no inhibition of these isoforms. However, 5,8,11-heptadecatriynoic acid methyl ester demonstrated inhibition specifically against one isoform (CYP1A2).

The toxicity evaluation through the ProTox-II webserver indicated the absence of hepatotoxic, carcinogenic, immunotoxic, and mutagenic activity in the studied compounds. Bisabolol oxide A demonstrated a non-toxic classification (rank 6) with a notably high LD_{50} of 8000 mg/kg; in contrast, bisabolol oxide B and 5,8,11-heptadecatriynoic acid methyl ester were categorized as low-toxic (rank 5), with LD_{50} values of 5000 mg/kg and 3881 mg/kg, respectively (Table 7).

Discussion

In recent years, natural substances have garnered significant attention for their broad-spectrum effects on both mental and physical well-being. Traditional medicine has long employed specific herbal compounds to enhance immune function and treat various pathologies [58–60]. Components derived from chamomile flowers are particularly recognized for their established anti-inflammatory, antioxidant, and anticancer properties, suggesting promising therapeutic potential [61]. Our findings indicate that bisabolol oxide A, bisabolol oxide B, and 5,8,11-heptadecatriynoic acid methyl ester, all chamomile derivatives potentially target key proteins integral to cell migration, namely β-catenin and EGFR. Furthermore, the incorporation of bisabolol oxide A into micellar/liposomal nanoparticles produced a significant modulation of gene expression in DU-145 prostate cancer cells. Specifically, this formulation upregulates pro-apoptotic genes (*P53* and *CASP9*) while concurrently downregulating genes associated with cell migration, including *β-catenin, SMAD3,* and *EGFR*. These results collectively underscore the therapeutic promise of bisabolol oxide A, establishing it not only as an intrinsic anticancer agent but also as a highly promising candidate for targeted cancer therapy when formulated within nanoparticle-based delivery systems.

The anticancer activity of herbal derivatives continues to be a focus of bio-researcher. For instance, curcumin, the principal component of Curcuma longa demonstrated enhanced anticancer efficacy against HT-29 colon cancer cells following encapsulation in polymersome nanocarriers, achieving IC_{50} values of 14, 10.6, and 9.8 µg/ml after 24, 48 and 72 hours, respectively [62]. Similarly, the ethanolic extract of *Rhabdosciadium microcalycinum* decreased the viability of A549 cells in a dose-dependent manner, exhibiting an IC_{50} of 117.15 µg/mL [63]. In related studies, Akkus et al. demonstrated that phenolic compounds, including 4-hydroxy-3-methoxyacetophenone, doxycycline hydrochloride and 5,7-dichloro-8 hydroxyquinoline, resulted in IC_{50} values of >100, 93.7 and 81.4 µg/mL, respectively, after 72 hour treatment on U2OS osteosarcoma cells [64]. Furthermore, Erdogan et al. reported an IC50 value of 324.2 µg/mL for the ethanolic extract of *Cephalaria elazigensis* var. *purpurea* against MCF-7 cancer cells [65]. Mousavi Eshkelani et al. reported that Quercetin-functionalized Ag_2O nanoparticles inhibited cell proliferation in DU-145 cancer cells, yielding IC_{50} values of 55.27, 43.34 and 12.79 µg/mL after 24, 48 and 72 hours, respectively. These nanoparticles also demonstrated a reduction in cell viability of up to 20% at concentrations ≤ 100 µg/mL after

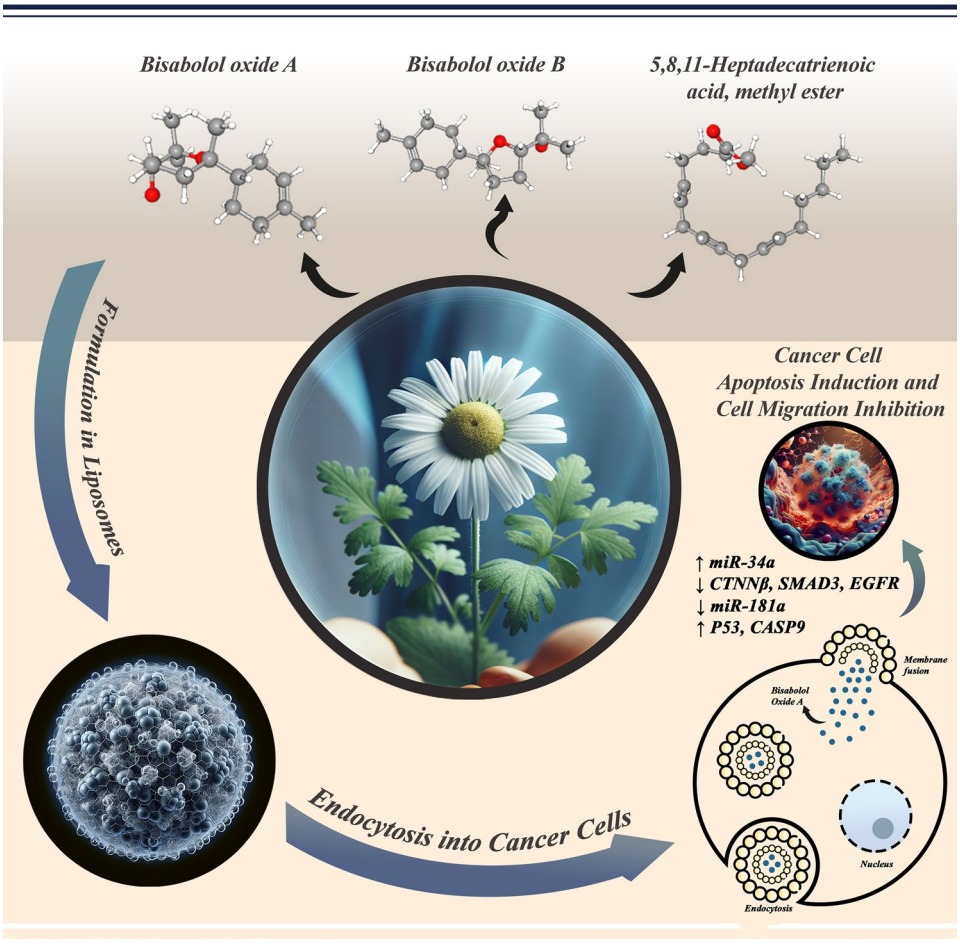

Fig. 10 Proposed mechanistic model of bisabolol oxide A-loaded nanoparticles. **a**) Primary bioactive components of chamomile used in this study. **b**) Schematic representation of the encapsulation process and the subsequent cellular effects: the nanoparticle formulation delivers bisabolol oxide A, which modulates the expression of specific miRnas to inhibit cell migration and induce apoptosis

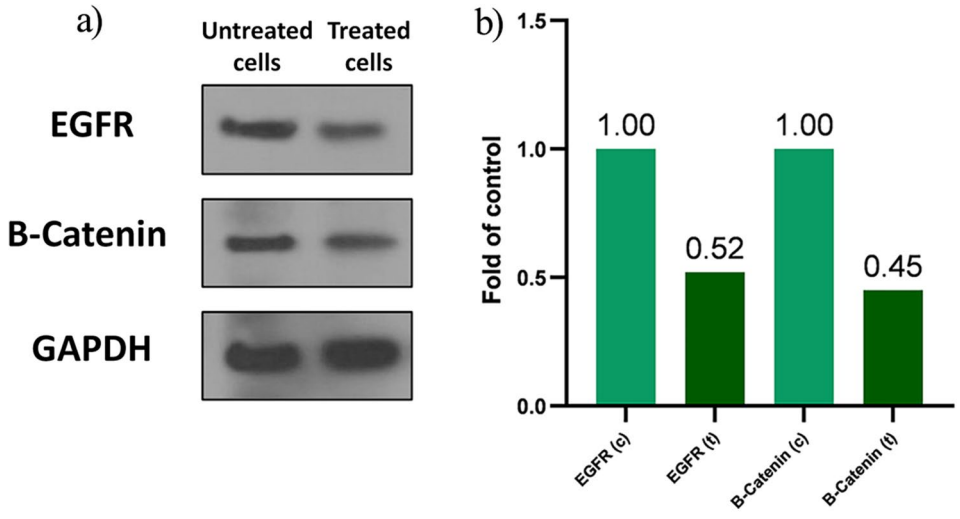

Fig. 11 Protein-level validation of key miR-34a targets following nanoparticle treatment in DU-145 cells. **a**) Representative Western blot images showing the reduction in EGFR and β-catenin protein expression after treatment with bisabolol oxide A-loaded micellar/liposomal nanoparticles (55.44 µg/mL). **b**) densitometric quantification of protein bands, presented as mean fold-changes ± SD relative to the untreated control. Statistical significance is indicated (e.g., $*p < 0.05$, $**p < 0.01$, $***p < 0.001$)

Table 4 Binding affinities and interacting residues governed by "β-catenin-ligands" and "EGFR-ligands" complexes

Compound name	β-catenin					EGFR				
	Binding affinity (kcal/mol)	No. of H-bonds	Residues forming H-bonds	No. of hydrophobic bonds	Residues forming hydrophobic	Binding affinity (kcal/mol)	No. of H-bonds	Residues forming H-bonds	No. of hydrophobic bonds	Residues forming hydrophobic
Bisabolol Oxide A	−6	2	Arg376, Trp338	7	Tyr306, Arg342, Lys345, Val346, Arg376, Trp383	−5.9	1	Arg841	10	Leu718, Val726, Ala743, Leu792, Met793, Leu844
Bisabolol Oxide B	−5.7	3	Arg469, Ser473, Asn516	4	Arg469, Lys508, Val511	−6.6	1	Thr854	9	Leu718, Val726, Lys745, Leu844
5,8,11-Heptadecatriynoic acid methyl ester	−4.8	3	Trp338, Arg342, Asn380	9	Tyr306, Trp338, Arg342, Lys345, Val349, Trp383	−5.2	5	Leu798, Leu799, Asp800, Arg841	9	Leu718, Val726, Ala743, Lys745, Arg841, Leu844

24 hours [66]. Further supporting the utility of nanocarriers, the IC50 of an Fe_3O_4@SP@Curcumin nanocomposite on AGS cells was determined to be 18.81, 15.26, and 9.91 µg/mL after 24, 48 and 72 hours, respectively. Importantly, the non-toxic profile of this nanocomposite was confirmed on HFF-2 normal fibroblast cells, showing cell viability > 80% at concentrations ≤ 100 µg/mL [67]. In the present study, bisabolol oxide A-loaded micellar/liposomal nanoparticles exhibited anti-proliferation effects on DU-145 prostate cancer cells with IC_{50} values of 55.44 µg/mL, 46.21 µg/mL, and 43.59 µg/mL at 24, 48, and 72 hours, respectively. Our findings concerning the dose- and time-dependent effects on DU-145 cells are consistent with those reported for quercetin and greater effectiveness than Paclitaxel (a chemotherapeutic agent). While the anti-proliferative function of bisabolol oxide A proved superior to that of the ethanolic extract and phenolic compounds tested, the efficacy of curcumin against HT-29 cells was found to be greater than that of bisabolol oxide A. Moreover, the non-toxic nature of bisabolol oxide A-loaded micellar/liposomal nanoparticles on HFF-2 normal cells was further confirmed by the MTT assay over the 3-day period. In addition, the nontoxic effect of empty PEG400-OA noncarriers was confirmed on both HFF-2 normal cells and DU-145 prostate cancer cells.

Apoptosis induction is a critical mechanism of action for anticancer drugs. Rasaei et al. demonstrated that a novel indole derivative (2Cl-5N-ind-dione) with an IC_{50} value of 70.54 µg/mL, induced apoptosis in HT-29 cells up to 28.23% after 24 hours [68]. In another study, Khakinezhad Tehrani et al. reported that silibinin encapsulated in polymersomes, at doses of 30, 40 and 50 µg/mL, induced apoptosis MIA PaCa-2 pancreatic cancer cells by 15.61%, 43.59% and 94.53%, respectively [69]. Our findings indicate that bisabolol oxide A-loaded micellar/liposomal nanoparticles induced apoptosis by 50.7% and 77.2% at concentrations 55.44 µg/mL (=IC_{50}), and 85.44 µg/mL in DU-145 cancer cells after 24 hours, suggesting this component exhibits apoptotic induction potential comparable to silibinin and superior to the indole derivative compound. It is noteworthy that both silibinin and bisabolol oxide A were incorporated into nanocarriers, a factor that likely facilitated enhanced or accelerated drug release and subsequent apoptosis induction.

Metastasis, a hallmark of tumorigenesis, is characterized by cancer cell migration from the primary tumor to secondary sites [70]. Pourasgar et al. demonstrated that curcumin-functionalized silica-coated Fe_3O_4 magnetic nanoparticles inhibited cell migration in AGS cancer cells by 18.81 µg/mL after 24 hours [67]. Mousavi Eshkelani et al. reported that Ag_2O@SP@Apigenin at a concentration of 41.45 µg/mL, inhibited AGS cell migration by 57% after 24 hours [71]. Furthermore, Al-Samydai et al. revealed

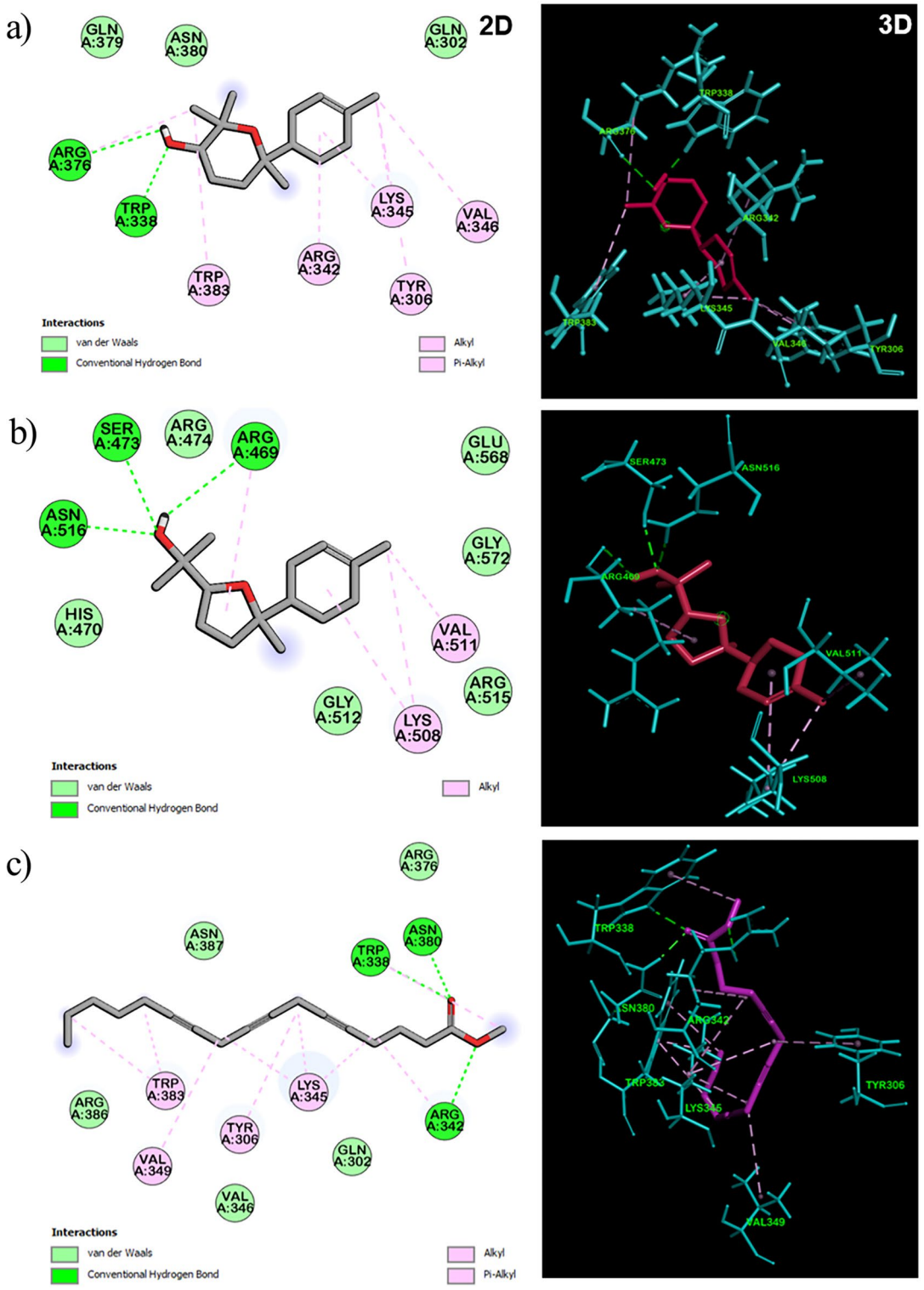

Fig. 12 2D/3D schematic representation of chemical interaction space governed by **a**) β-catenin and bisabolol oxide A, **b**) bisabolol oxide **B**, and **c**) methyl ester 5,8,11-heptadecatriynoic acid

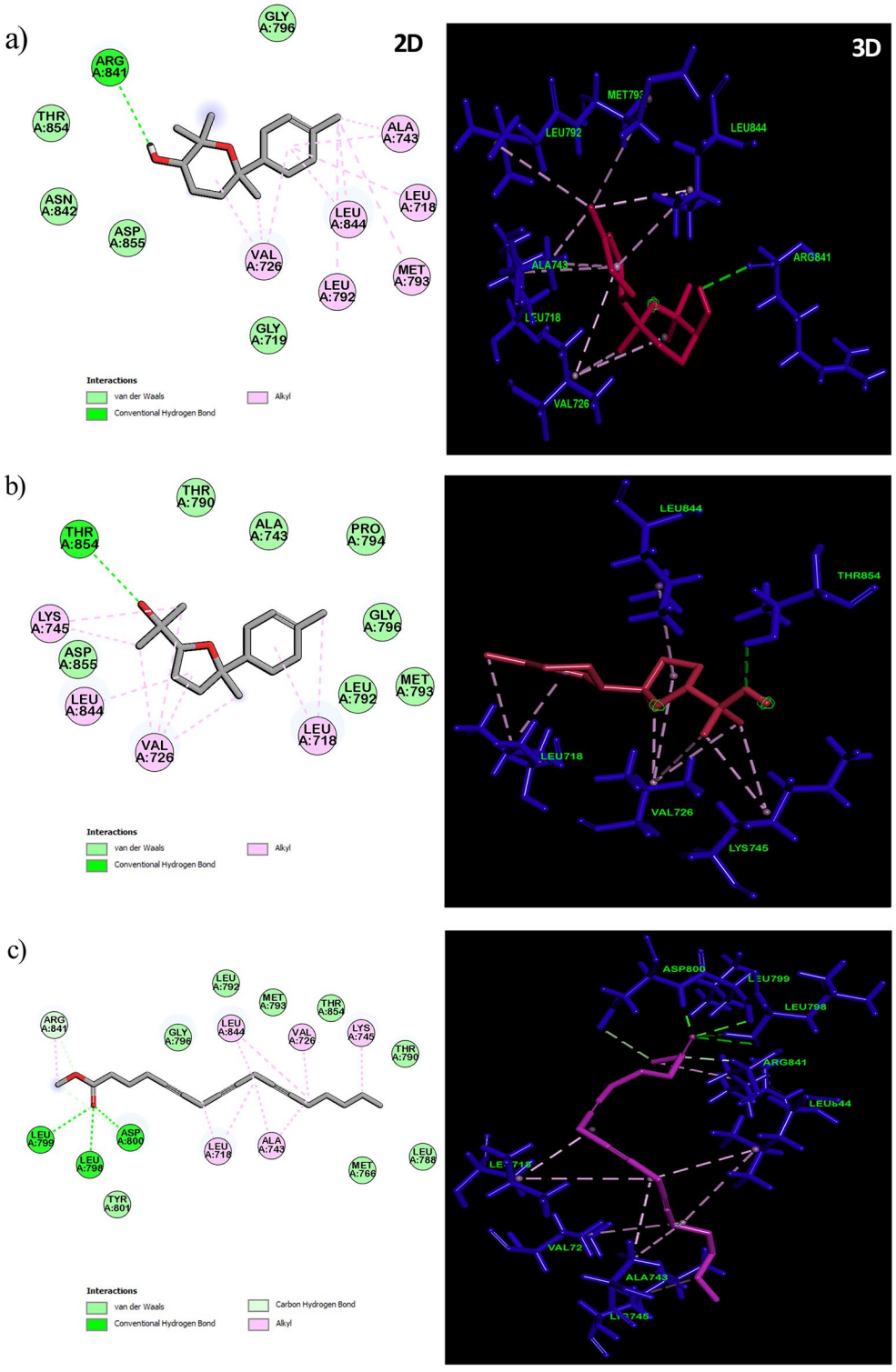

Fig. 13 2D/3D schematic representation of chemical interaction space governed by **a**) EGFR and bisabolol oxide A, **b**) bisabolol oxide B, and **c**) methyl ester 5,8,11-heptadecatriynoic acid

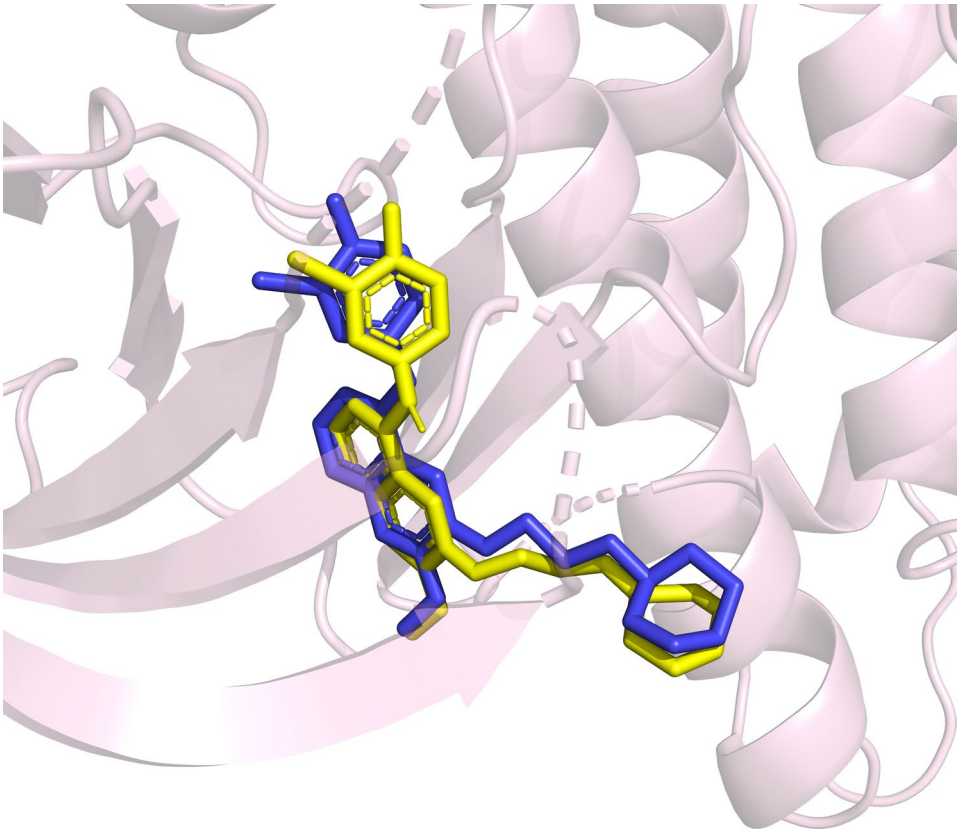

Fig. 14 Superimposition of crystallized and redocked gefitinib in the active site of EGFR. Native gefitinib is shown in blue, and docked gefitinib in yellow

Table 5 Drug-like properties of studied compounds according to Lipinski's rule of five

ID	Compound Name	MW	NHBD	NHBA	LogP
1	Bisabolol Oxide A	238.37	1	2	2.70
2	Bisabolol Oxide B	238.37	1	2	2.70
3	5,8,11-Heptadecatriynoic acid methyl ester	272.38	0	2	4.38

MW: molecular weight, NHBD: number of hydrogen bond donors, NHBA: number of hydrogen bond acceptors, LogP: octanol/water partition coefficient.

that PEGylated nanophytosome 6-gingerol inhibited cell migration by >50% in human periodontal ligament fibroblasts after 24 hours [72]. Amin et al. showed that Saffron and its major ingredients possess inhibitory effects on colon cancer cell migration [73]. In the present study, bisabolol oxide A inhibited cell migration by approximately 50.04% DU-145 cancer cells after 24 hours, confirming previous findings and highlighting the multifunctional effects of this component on DU-145 cancer cells.

In silico analysis has predicted that 30% to 60% of mammalian genes may be regulated by microRNAs (miRNAs) [74]. Aslani et al. reported that crocin, an active compound in saffron, reduced the expression of miR-181a in HELA/Ara-C cell lines while concurrently increasing the expression of miR-34a in PTC cells [75]. Su et al. demonstrated that miR-34a, a known tumor-suppressive miRNA, inhibits tumorigenesis by regulating the Axl/Akt/GSK-3β pathway, thereby affecting downstream genes such as *c-Myc* and *β-catenin* [76]. Furthermore, Yu et al. revealed that onco-miR181a increases the protein levels of CDC25A and the anti-apoptotic protein Bcl-2 while decreasing the pro-apoptotic protein Bax in gastric cancer cells [77]. Moreover, Sun et al. showed that onco-miR-181a induces angiogenesis in colorectal cancer, suggesting that miR-181a could serve as a potential therapeutic target [16]. Our findings demonstrated the upregulation of the tumor-suppressive miR-34a and the downregulation of onco-miR-181a in DU-145 prostate cancer cells treated with bisabolol oxide A-loaded polymeric nanoparticles. Thus, bisabolol oxide A shows promise as a therapeutic agent against cancer migration and angiogenesis, partly through the regulatory mechanism involving the upregulation of miR-34a and downregulation of miR-181a.

Pakizehkar et al. demonstrated that curcumin encapsulated in polymersomes inhibited cell migration in MDA-MB-231 human breast cancer cells [78]. Chen et al. reported that a plant-based medicinal food (PBMF) composed of six medicinal and edible plants induced apoptosis in SGC-7901 gastric cancer cells by upregulating E-*cadherin, Bax, caspase-3,* and *caspase*-9, while downregulating *β-catenin, MMP-2,* and *MMP-9* [79].

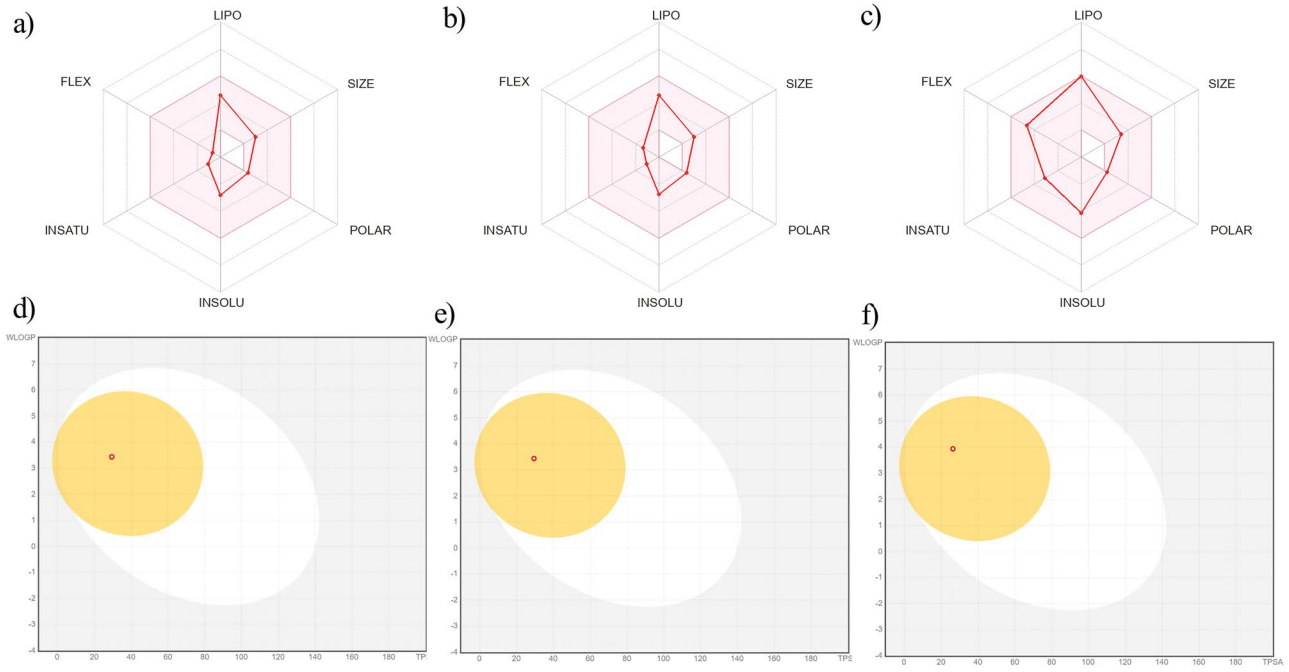

Fig. 15 Prediction of bioavailability and blood-brain barrier (BBB) permeability for selected compounds. **a**) bioavailability radar plot of bisabolol oxide A. **b**) bioavailability radar plot of bisabolol oxide B. **c**) bioavailability radar plot of 5,8,11-heptadecatriyn-1-oic acid methyl ester. The pink region exhibits the ideal range for oral bioavailability parameters. The red lines illustrate the predicted physicochemical properties of compounds. **d**) BOILED-Egg model for bisabolol oxide A. **e**) BOILED-Egg model for bisabolol oxide B. **f**) BOILED-Egg model for 5,8,11-heptadecatriyn-1-oic acid methyl ester. Points located in the yolk (yellow region) represent molecules capable of BBB permeation, whereas points in the albumin (white area) represent passive absorption by the gastrointestinal tract. The red color of spots indicates molecules that cannot be effluxed from the central nervous system (CNS) by P-glycoprotein. LIPO: lipophilicity (between −0.7 and +5.0), SIZE: molecular weight (between 150 and 500 g/mol), POLAR: polarity (between 20 and 130 $Å^2$), INSOLU: solubility (not higher than 6), NSATU: saturation (fraction of carbons in the sp^3 hybridization not less than 0.25), FLEX: flexibility (no more than 9 rotatable bonds)

Table 6 Pharmacokinetic properties of studied compounds

ID	Compound Name	TPSA	Log S	GI absorption	BBB permeant	P-gp substrate
1	Bisabolol Oxide A	29.46	Soluble	High	Yes	No
2	Bisabolol Oxide B	29.46	Soluble	High	Yes	No
3	5,8,11-Heptadecatriynoic acid methyl ester	26.30	Moderately soluble	High	Yes	No

TPSA: topological polar surface area, Log S: solubility, GI absorption: gastrointestinal absorption, BBB permeant: blood-brain barrier permeability, P-gp substrate: P-glycoprotein substrate

Table 7 Toxicity indices of chemical compounds

Compound Name	LD_{50} Score (mg/kg)	HT	CG	IT	MG	CT	TC
Bisabolol oxide A	8000	Inactive	Inactive	Inactive	Inactive	Inactive	6
Bisabolol oxide B	5000	Inactive	Inactive	Inactive	Inactive	Inactive	5
5,8,11-heptadecatriynoic acid methyl ester	3881	Inactive	Inactive	Inactive	Inactive	Inactive	5

LD_{50}; fifty percent lethal dose (mg/kg); HT, hepatotoxicity; CG, carcinogenicity; IT, immunotoxicity; MG, mutagenicity; CT, cytotoxicity; TC, toxicity class.

Our findings suggest that bisabolol oxide A encapsulated in micellar/liposomal nanoparticles and known as a key component of chamomile, can inhibit cell migration and invasion at both the transcriptional and translational levels. This inhibition is achieved by modulating genes and proteins such as EGFR and β-catenin, which are potential targets of miR-34a.

Silibinin, derived from *Silybum marianum*, when encapsulated in polymersomes at a dose of 50 µg/mL, was shown to induce apoptosis, DNA fragmentation, and the overexpression of *P53, CASP9, APAF1,* and *BAX* genes in PANC-1 cells [80]. Similarly, catechin, a compound found in green tea, induces apoptotic cell death in various malignant B-cell lines through the release of cytochrome c and the subsequent activation of *caspase-3* and *caspase-9* [81]. Furthermore, curcumin has been reported to induce apoptosis and inhibit autophagy in human gastric cancer cell lines (BGC-823, SGC-7901, and MKN-28) in a time- and dose-dependent manner [82]. In our study, we observed that bisabolol oxide A-loaded nanoparticles

effectively induced apoptosis in DU-145 cells and significantly increased the expression of key apoptotic genes, including *P53* and *CASP9*, which are potential targets of miR-181a. These findings strongly suggest the therapeutic potential of bisabolol oxide A in cancer treatment.

Chamomile is recognized as one of the oldest medicinal herbs, containing over 120 constituents in its essential oil. Among these, α-(−)-bisabolol, bisabolol oxides A and B, chamazulene, and β-farnesene are considered key compounds [83]. Molecular docking analysis have demonstrated high binding affinities of certain chamomile-derived compounds, specifically bisabolol oxides A and B and 5,8,11-heptadecatriynoic acid methyl ester, for β-catenin and EGFR. Shaik et al. reported that a chemical analogue of edible curcumin (CUCM36) exhibited a stronger affinity for both wild-type and mutant forms of EGFR (V769L & K846R; ΔG for both > −9.20 kcal/mol) compared to natural curcumin [84]. Similarly, in silico docking analysis by Razak et al. indicated that an indole derivative predicted binding to GPx, COX2, IL1, and NF-κB [85]. Our study aligns with previous findings, demonstrating interactions between chamomile-derived compounds and key amino acid residues. Notably, the E-cadherin/β-catenin complex plays a critical role in cell-cell adhesion [86]. This suggests that chamomile compounds may target E-cadherin interaction sites on β-catenin, thereby potentially inhibiting tumor cell adhesion. Yan et al. previously showed that EGFR binds to its inhibitor (CO-1686) via hydrophobic residues Leu718, Val726, and Leu844, and mutation in these residues disrupted the EGFR/CO-1686 interaction [87]. Consistent with our study observed interactions between bisabolol oxide A, bisabolol oxide B, and 5,8,11-heptadecatriynoic acid methyl ester with EGFR at these critical residues, further highlighting their potential as therapeutic agents targeting EGFR-mediated pathways.

Despite the promising findings, this study has several limitations. First, all biological evaluations were conducted in vitro using the DU-145 prostate cancer cell line. Consequently, the therapeutic efficacy and biosafety of bisabolol oxide A-loaded nanoparticles require further validation in appropriate in vivo models. Moreover, additional mechanistic investigations and pharmacokinetic assessments are necessary to comprehensively elucidate the translational potential of this nanoparticle-based delivery system.

Conclusion

This study suggests that nanoparticles containing bisabolol oxide A exhibit particle sizes ranging from 35 to 67 nm, a uniform distribution, and thermal stability up to 380 °C. While current nanoparticle-based drug delivery and BECC screening strategies have been valuable for improving drug solubility, stability, and cytotoxicity, they are often limited to physicochemical characterization and phenotypic cellular assays, such as viability, apoptosis, or migration inhibition. Such conventional approaches may lack mechanistic depth, particularly in relation to post-transcriptional regulatory networks, including miRNA-mediated gene regulation. Here, we propose an integrated framework that combines nanoparticle formulation with molecular-level mechanistic investigation. Our findings indicate that bisabolol oxide A-loaded micellar/liposomal nanoparticles can reduce proliferation and migration in DU-145 prostate cancer cells and may modulate tumorsuppressive and oncogenic miRNAs (miR-34a and miR-181a). Furthermore, this miRNA deregulation appears to correlate with downstream changes in key protein targets, including β-catenin and EGFR, at both transcriptional and translational levels. Although additional in vivo and clinical validation would be necessary to confirm these findings, the present results provide preliminary mechanistic insights into a potential miRNA–gene–protein regulatory axis influenced by bisabolol oxide-A nanoparticle delivery. This approach may offer a promising direction for future explorations of nanoparticle-mediated anticancer mechanisms.

Abbreviations

ADME	Absorption, Distribution, Metabolism, and Excretion
APAF1	Apoptotic Peptidase Activating Factor 1
CASP	Caspase
CTNNB1	Catenin Beta 1
EGFR	Epidermal Growth Factor Receptor
FT-IR	Fourier-Transform Infrared Spectroscopy
GI	Gastrointestinal
IC_{50}	Half-Maximal Inhibitory Concentration
MD	Molecular Dynamics
miRNA	MicroRNA
PEG	Polyethylene Glycol
qRT-PCR	Quantitative Real-Time Polymerase Chain Reaction
SEM	Scanning Electron Microscopy
TEM	Transmission Electron Microscopy
TGA-DTG	Thermogravimetric Analysis–Differential Thermogravimetry

Supplementary Information

The online version contains supplementary material available at https://doi.org/10.1186/s12896-026-01168-4.

Supplementary material 1

Acknowledgements

Y. N. Ertas acknowledges support from the Turkish Academy of Sciences (TÜBA). The authors appreciate the support from Islamic Azad University, Rasht Branch.

Author contributions

M.N., N.R., B.R., and Y.N.E. contributed to the conception and design of the study. S.F.K., Z.A.K., F.B.F., S. N.C., A.N.K., and H.Z. collected, analyzed, and interpreted the data. N.R., M.S., and S.F.K. performed statistical analyses. Z.A.K., M.N., N.R., M.S., H.Z., B.R., and Y.N.E. drafted and critically revised the manuscript. N.R., M.N., M.S., H.Z., and Y.N.E. approved the final version. Z.A.K. prepared the TOC graphic, created charts, organized figures, and performed final formatting.

Funding
No funding was obtained for this study.

Data availability
All datasets generated and analyzed during this study are available from the corresponding author upon reasonable request. Computational data (docking and ADME files) and raw qRT-PCR output files can also be provided upon request.

Declarations

Ethics approval and consent to participate
Not applicable. This study did not involve human subjects, animal models, or clinical samples requiring ethics committee approval.

Consent for publication
Not applicable. No individual person's data or identifying information is included in this study.

Competing interests
The authors declare no competing interests.

Author details
[1]Department of Biology, Ra.C., Islamic Azad University, Rasht, Iran
[2]Department of Chemical Engineering, Amirkabir University of Technology (Tehran Polytechnic), 424 Hafez Avenue, Tehran, Iran
[3]Department of Microbiology, La.C., Islamic Azad University, Lahijan, Iran
[4]Department of Biology, University of Guilan, Rasht, Iran
[5]Department of Chemistry, Ra.C., Islamic Azad University, Rasht, Iran
[6]Department of Biomedical Engineering, Erciyes University, Kayseri 38039, Türkiye

Received: 11 November 2025 / Accepted: 7 May 2026
Published online: 23 May 2026

References

1. Ogata-Ikeda I, Seo H, Kawanai T, Hashimoto E, Oyama Y. Cytotoxic action of bisabololoxide a of German chamomile on human leukemia K562 cells in combination with 5-fluorouracil. Phytomedicine. 2011;18(5):362–65. https://doi.org/10.1016/j.phymed.2010.08.007.
2. Srivastava G. Chamomile: a herbal medicine of the past with a bright future (review). Mol Med Rep. 2010;3(6):895–901. https://doi.org/10.3892/mmr.2010.377.
3. Singh O, Khanam Z, Misra N, Srivastava MK. Chamomile (Matricaria chamomilla L.): an overview. Phcog Rev. 2011;5(9):82–95. https://doi.org/10.4103/0973-7847.79103.
4. Sah A, Naseef PP, Kuruniyan MS, Jain GK, Zakir F, Aggarwal G. A comprehensive study of therapeutic applications of chamomile. Pharmaceuticals. 2022;15(10):1284. https://doi.org/10.3390/ph15101284.
5. Das S, Horváth B, Šafranko S, Jokić S, Széchenyi A, Kőszegi T. Antimicrobial activity of chamomile essential oil: effect of different formulations. Molecules. 2019;24(23):4321. https://doi.org/10.3390/molecules24234321.
6. Sak K, Nguyen TH, Ho VD, Do TT, Raal A. Cytotoxic effect of chamomile (Matricaria recutita) and marigold (calendula officinalis) extracts on human melanoma SK-MEL-2 and epidermoid carcinoma KB cells. Cogent Med. 2017;4(1):1333218. https://doi.org/10.1080/2331205X.2017.1333218.
7. Park J, Han F, Lee IS. Biotransformation of (−)-α-bisabolol by Absidia coerulea. Molecules. 2022;27(3):881. https://doi.org/10.3390/molecules27030881.
8. Biltekin SN, Karadağ AE, Demirci F, Demirci B. In vitro anti-inflammatory and anticancer Evaluation of Mentha spicata L. and Matricaria chamomilla L. Essential Oils. Essent Oils. ACS Omega. 2023;8(19):17143–50. https://doi.org/10.1021/acsomega.3c01501.
9. Su YQ, Lu Y, An HL, Liu JH, Ye FM, Shen JY, et al. MicroRNA-204-5p inhibits hepatocellular carcinoma by targeting the regulator of G protein signaling 20. ACS Pharmacol Transl Sci. 2023;6(12):1817–28. https://doi.org/10.1021/acsptsci.3c00114.
10. Nemeth K, Bayraktar R, Ferracin M, Calin GA. Non-coding RNAs in disease: from mechanisms to therapeutics. Nat Rev Genet. 2024;25(3):211–32. https://doi.org/10.1038/s41576-023-00662-1.
11. Paskeh MDA, Mirzaei S, Orouei S, Zabolian A, Saleki H, Azami N, et al. Revealing the role of miRNA-489 as a new onco-suppressor factor in different cancers based on pre-clinical and clinical evidence. Int J Biol Macromolecules. 2021;191:727–37. https://doi.org/10.1016/j.ijbiomac.2021.09.089.
12. Balasundaram A, Mitra TS, Tayubi IA, Zayed H, Doss GPC. Deciphering the miRNA–mRNA interaction landscape between breast cancer and triple-Negative breast cancer: an integrated Bioinformatics approach. ACS Omega. 2024;9(23):24379–95. https://doi.org/10.1021/acsomega.4c00011.
13. Otmani K, Rouas R, Berehab M, Lewalle P. The regulatory mechanisms of oncomiRs in cancer. Biomed Pharmacother. 2024;171:171. https://doi.org/10.1016/j.biopha.2024.116165.
14. Abdelaal AM, Sohal IS, Iyer S, Sudarshan K, Kothandaraman H, Lanman NA, et al. A first-in-class fully modified version of miR-34a with outstanding stability, activity, and anti-tumor efficacy. Oncogene. 2023;42(40):2985–99. https://doi.org/10.1038/s41388-023-02801-8.
15. Gupta J, Suliman M, Ali R, Margiana R, Hjazi A, Alsaab HO, et al. Double-edged sword role of miRNA-633 and miRNA-181 in human cancers. Pathol - Res Pract. 2023;248:248. https://doi.org/10.1016/j.prp.2023.154701.
16. Sun W, Wang X, Li J, You C, Lu P, Feng H, et al. MicroRNA-181a promotes angiogenesis in colorectal cancer by targeting SRCIN1 to promote the SRC/VEGF signaling pathway. Cell Death Dis. 2018;9(4):438. https://doi.org/10.1038/s41419-018-0490-4.
17. Pallavi P, Harini K, Gowtham P, Girigoswami K, Girigoswami A. Fabrication of polymersomes: a macromolecular architecture in Nanotherapeutics. Chemistry. 2022;4(3):1028–43. https://doi.org/10.3390/chemistry4030070.
18. Gao W, Bigham A, Ghomi M, Zarrabi A, Rabiee N, Saeb MR, et al. Micelle-engineered nanoplatforms for precision oncology. Chem Eng-New Y J. 2024;495:495. https://doi.org/10.1016/j.cej.2024.153438.
19. Almajidi YQ, Kadhim MM, Alsaikhan F, Jalil AT, Sayyid NH, Ramírez-Coronel AA, et al. Doxorubicin-loaded micelles in tumor cell-specific chemotherapy. Environ Res. 2023;227:227. https://doi.org/10.1016/j.envres.2023.115722.
20. Tang M, Song JZ, Zhang SY, Shu XL, Liu S, Ashrafizadeh M, et al. Innovative theranostic hydrogels for targeted gastrointestinal cancer treatment. J Transl Med. 2024;22(1). https://doi.org/10.1186/s12967-024-05749-9.
21. Li TF, Ashrafizadeh M, Shang YR, Ertas YN, Orive G. Chitosan-functionalized bioplatforms and hydrogels in breast cancer: immunotherapy, phototherapy and clinical perspectives. Drug Discov. Today Today. 2024;29(1):103851. https://doi.org/10.1016/j.drudis.2023.103851.
22. Dai JY, Ashrafizadeh M, Aref AR, Sethi G, Ertas YN. Peptide-functionalized, -assembled and - loaded nanoparticles in cancer therapy. Drug Discov. Today Today. 2024;29(7):103981. https://doi.org/10.1016/j.drudis.2024.103981.
23. Li Y, Ertas YN, Jafari A, Taheri M, Pilehvar Y. Co-delivery of curcumin and chrysin through pH-sensitive hyaluronan-modified hollow mesoporous silica nanoparticles for enhanced synergistic anticancer efficiency against thyroid cancer cells. J Drug Delivery Sci Technol. 2023;87:87. https://doi.org/10.1016/j.jddst.2023.104787.
24. Yildiz SN, Entezari M, Paskeh MDA, Mirzaei S, Kalbasi A, Zabolian A, et al. Nanoliposomes as nonviral vectors in cancer gene therapy. Medcomm. 2024;5(7). https://doi.org/10.1002/mco2.583.
25. Hashemi M, Ghadyani F, Hasani S, Olyaee Y, Raei B, Khodadadi M, et al. Nanoliposomes for doxorubicin delivery: reversing drug resistance, stimuli-responsive carriers and clinical translation. J Drug Delivery Sci Technol. 2023;80:80. https://doi.org/10.1016/j.jddst.2022.104112.
26. Ashrafizadeh M, Zarrabi A, Bigham A, Taheriazam A, Saghari Y, Mirzaei S, et al. (Nano)platforms in breast cancer therapy: Drug/gene delivery, advanced nanocarriers and immunotherapy. Med Res Rev. 2023;43(6):2115–76. https://doi.org/10.1002/med.21971.
27. Entezari M, Abad GGY, Sedghi B, Ettehadi R, Asadi S, Beiranvand R, et al. Gold nanostructure-mediated delivery of anticancer agents: biomedical applications, reversing drug resistance, and stimuli-responsive nanocarriers. Environ Res. 2023;225:225. https://doi.org/10.1016/j.envres.2023.115673.
28. Bagheri M, Zandieh MA, Daryab M, Samaei SS, Gholami S, Rahmanian P, et al. Nanostructures for site-specific delivery of oxaliplatin cancer therapy: versatile nanoplatforms in synergistic cancer therapy. Transl Oncol. 2024;39:39. https://doi.org/10.1016/j.tranon.2023.101838.
29. Letchford K, Burt H. A review of the formation and classification of amphiphilic block copolymer nanoparticulate structures: micelles, nanospheres, nanocapsules and polymersomes. Eur J Criminol Pharm Biopharmaceutics. 2007;65(3):259–69. https://doi.org/10.1016/j.ejpb.2006.11.009.
30. Stoletov K, Beatty PH, Lewis JD. Novel therapeutic targets for cancer metastasis. Expert Rev Anticancer Ther. 2020;20(2):97–109. https://doi.org/10.1080/14737140.2020.1718496.

31. Hashemi M, Hajimazdarany S, Mohan CD, Mohammadi M, Rezaei S, Olyaee Y, et al. Long non-coding RNA/epithelial-mesenchymal transition axis in human cancers: tumorigenesis, chemoresistance, and radioresistance. Pharmacological Res. 2022;186:186. https://doi.org/10.1016/j.phrs.2022.106535.
32. Sabouni E, Nejad MM, Mojtabavi S, Khoshdooz S, Mojtabavi M, Nadafzadeh N, et al. Unraveling the function of epithelial-mesenchymal transition (EMT) in colorectal cancer: metastasis, therapy response, and revisiting molecular pathways. Biomed Pharmacother. 2023;160:160. https://doi.org/10.1016/j.biopha.2023.114395.
33. Ebrahimi N, Manavi MS, Faghihkhorasani F, Fakhr SS, Baei FJ, Khorasani FF, et al. Harnessing function of EMT in cancer drug resistance: a metastasis regulator determines chemotherapy response. Cancer Metastasis Rev. 2024;43(1):457–79. https://doi.org/10.1007/s10555-023-10162-7.
34. Barcelona-Estaje E, Dalby MJ, Cantini M, Salmeron-Sanchez M. You talking to me? Cadherin and Integrin crosstalk in biomaterial design. Adv Healthcare Mater. 2021;10(6). https://doi.org/10.1002/adhm.202002048.
35. Tian X, Liu Z, Niu B, Zhang J, Tan TK, Lee SR, et al. E-cadherin/β-catenin complex and the epithelial barrier. Biomed Res Int. 2011;2011(1):567305. https://doi.org/10.1155/2011/567305.
36. Polyak K, Weinberg RA. Transitions between epithelial and mesenchymal states: acquisition of malignant and stem cell traits. Nat Rev Cancer. 2009;9(4):265–73. https://doi.org/10.1038/nrc2620.
37. Shang S, Hua F, Hu ZW. The regulation of β-catenin activity and function in cancer: therapeutic opportunities. Oncotarget. 2017;8(20):33972–89. https://doi.org/10.18632/oncotarget.15687.
38. Shou YF, Teo XY, Wu KZ, Bai BY, Kumar ARK, Low J, et al. Dynamic stimulations with bioengineered extracellular Matrix-mimicking hydrogels for mechano cell reprogramming and therapy. Adv Sci. 2023;10(21). https://doi.org/10.1002/advs.202300670.
39. Indongo G, Madanan AS, Varghese S, Shkhair AI, Abraham MK, Rajeevan G, et al. Exploring selective fluorescence turn-on sensing of Caspase-3 with molybdenum disulfide quenched copper nanoclusters: FRET biosensor. ACS Appl Mater Interface. 2024;16(45):61599–608. https://doi.org/10.1021/acsami.4c10967.
40. Xu HD, Cheng XT, Sun XB, Chen PY, Zhan WJ, Liu XY, et al. Caspase-3-Triggered Intracellular Gadolinium nanoparticle formation for T 1 -Weighted Magnetic Resonance Imaging of apoptosis in vivo. Nano Lett. 2023;23(13):6178–83. https://doi.org/10.1021/acs.nanolett.3c01787.
41. Sahoo G, Samal D, Khandayataray P, Murthy MK. A review on caspases: key regulators of biological Activities and apoptosis. Mol Neurobiol. 2023;60(10):5805–37. https://doi.org/10.1007/s12035-023-03433-5.
42. Tait SWG, Green DR. Mitochondria and cell death: outer membrane permeabilization and beyond. Nat Rev Mol Cell Biol. 2010;11(9):621–32. https://doi.org/10.1038/nrm2952.
43. Zhou Z, Arroum T, Luo X, Kang R, Lee YJ, Tang DL, et al. Diverse functions of cytochrome c in cell death and disease. Cell Death Differ. 2024;31(4):387–404. https://doi.org/10.1038/s41418-024-01284-8.
44. Sadeghizadeh M, Tahmasebi Mirgani M, Sadeghizadeh I, Marra F, Bilia AR, Mowla SJ, et al. Dendrosomal curcumin nanoformulation downregulates pluripotency genes via miR-145 activation in U87MG glioblastoma cells. IJN. 2014;9:403–17. https://doi.org/10.2147/IJN.S48136.
45. Colak B, Ertas YN. Implantable, 3D-Printed alginate scaffolds with bismuth sulfide nanoparticles for the treatment of local breast cancer via enhanced radiotherapy. ACS Appl Mater Interface. 2024;16(13):15718–29. https://doi.org/10.1021/acsami.3c17024.
46. Yaray K, Norbakhsh A, Rashidzadeh H, Mohammadi A, Mozafari F, Ghaffarlou M, et al. Chemoradiation therapy of 4T1 cancer cells with methotrexate conjugated platinum nanoparticles under X-Ray irradiation. Inorg Chem Commun. 2023;150:150. https://doi.org/10.1016/j.inoche.2023.110457.
47. Shin MJ, Im S, Kim B, Choi J, Lucia SE, Kim W, et al. Fabrication of scratched nanogrooves for highly oriented cell alignment and application as a wound healing dressing. ACS Appl Mater Interface. 2023;15(15):18653–62. https://doi.org/10.1021/acsami.3c00530.
48. Mashayekh E, Ghiasi ZNK, Bhia I, Khorrami ZA, Malekahmadi O, Bhia M, et al. Metal–organic frameworks for cisplatin delivery to cancer cells: a Molecular Dynamics simulation. ACS Omega. 2024;9(17):19627–36. https://doi.org/10.1021/acsomega.4c01437.
49. Tu G, Fu TT, Zheng GX, Xu BB, Gou RP, Luo D, et al. Computational Chemistry in structure-based solute carrier transporter drug Design: recent advances and future perspectives. J Chem Inf Model. 2024;64(5):1433–55. https://doi.org/10.1021/acs.jcim.3c01736.
50. Gasteiger J, Marsili M. Iterative partial equalization of orbital electronegativity—a rapid access to atomic charges. Tetrahedron. 1980;36(22):3219–28. https://doi.org/10.1016/0040-4020(80)80168-2.
51. Pettersen EF, Goddard TD, Huang CC, Couch GS, Greenblatt DM, Meng EC, et al. UCSF Chimera—A visualization system for exploratory research and analysis. J Comput Chem. 2004;25(13):1605–12. https://doi.org/10.1002/jcc.20084.
52. Esnaashari F, Rostamnejad D, Zahmatkesh H, Zamani H. In vitro and in silico assessment of anti-quorum sensing activity of Naproxen against Pseudomonas aeruginosa. World J Microbiol Biotechnol. 2023;39(9):244. https://doi.org/10.1007/s11274-023-03690-5.
53. Ni BY, Wang HY, Khalaf HKS, Blay V, Houston DR. AutoDock-SS: AutoDock for Multiconformational ligand-based virtual screening. J Chem Inf Model. 2024;64(9):3779–89. https://doi.org/10.1021/acs.jcim.4c00136.
54. Hossain KR, Turkewitz DR, Holt SA, Brun APL, Valenzuela SM. Sterol Structural features' impact on the spontaneous membrane insertion of CLIC1 into artificial lipid membranes. Langmuir. 2023;39(9):3286–300. https://doi.org/10.1021/acs.langmuir.2c03129.
55. Bazgosha M, Saberi GA, Hormozi M, Shirangi K, Shaghaghi Bahri F, Zahmatkesh H, et al. Augmentation of antibacterial activity of ciprofloxacin by bisabololoxide a encapsulated in polymeric nanoparticles against uropathogenic Escherichia coli. BMC Biotechnol. 2025;25(1):140. https://doi.org/10.1186/s12896-025-01070-5.
56. Manhas D, Dhiman S, Kour H, Kour D, Sharma K, Wazir P, et al. ADME/PK insights of Crocetin: a molecule having an unusual chemical structure with druglike features. ACS Omega. 2024;9(19):21494–509. https://doi.org/10.1021/acsomega.4c02116.
57. Daina A, Michielin O, Zoete V. SwissADME: a free web tool to evaluate pharmacokinetics, drug-likeness and medicinal chemistry friendliness of small molecules. Sci Rep. 2017;7(1):42717. https://doi.org/10.1038/srep42717.
58. Farzan M, Abedi B, Bhia I, Madanipour A, Farzan M, Bhia M, et al. Pharmacological Activities and Molecular mechanisms of sinapic acid in neurological disorders. ACS Chem. Neurosci. 2024;15(16):2966–81. https://doi.org/10.1021/acschemneuro.4c00349.
59. Zarepour A, Ülker Z, Khosravi A, Coskun A, Ertas YN, Yildiz M, et al. Light-responsive liposome as a smart vehicle for the delivery of anticancer herbal medicine to skin. Emergent Mater. 2025;8(2):959–70. https://doi.org/10.1007/s42247-024-00907-7.
60. Ashrafizadeh M, Aref AR, Sethi G, Ertas YN, Wang L. Natural product/diet-based regulation of macrophage polarization: implications in treatment of inflammatory-related diseases and cancer. The J Nutritional Biochem. 2024;130:130. https://doi.org/10.1016/j.jnutbio.2024.109647.
61. Karaca N, Demirci B, Gavahian M, Demirci F. Enhanced bioactivity of Rosemary, sage, lavender, and chamomile essential Oils by fractionation, combination, and emulsification. ACS Omega. 2023;8(12):10941–53. https://doi.org/10.1021/acsomega.2c07508.
62. Pakizehkar S, Ranji N, Sohi AN, Sadeghizadeh M. Polymersome-assisted delivery of curcumin: a suitable approach to decrease cancer stemness markers and regulate miRnas expression in HT29 colorectal cancer cells. Polym Adv Techs. 2020;31(1):160–77. https://doi.org/10.1002/pat.4759.
63. Erdogan MK, Gundogdu R, Yapar Y, Gecibesler IH, Kirici M, Behcet L, et al. The Evaluation of anticancer, antioxidant, antidiabetic and anticholinergic potentials of endemic Rhabdosciadium microcalycinum supported by Molecular docking study. ChemistrySelect. 2022;7(17):e202200400. https://doi.org/10.1002/slct.202200400.
64. Akkus M, Kirici M, Poustforoosh A, Erdogan MK, Gundogdu R, Tüzün B, et al. Phenolic compounds: investigating their anti-carbonic anhydrase, anti-Cholinesterase, anticancer, anticholinergic, and antiepileptic properties through Molecular docking, MM-GBSA, and Dynamics analyses. Korean J Chem Eng. 2025;42(5):1149–68. https://doi.org/10.1007/s11814-025-00401-8.
65. Erdogan MK, Gundogdu R, Yapar Y, Gecibesler IH, Kirici M, Behcet L, et al. In vitro anticancer, antioxidant and enzyme inhibitory potentials of endemic Cephalaria elazigensis var. purpurea with in silico studies. J Educ Chang Biomol Struct Dyn. 2023;41(21):11832–44. https://doi.org/10.1080/07391102.2022.2163700.
66. Eshkelani SMM, Hassankiadeh AS, Hajitabar M, Balasbaneh ZS, Kazemi T, Dafchahi HB, et al. Anti-invasion and apoptotic induction effects of Quercetin-functionalized silver oxide (Ag2O) nanoparticles on DU-145 prostate carcinoma cells via modulation of miR-34a, miR-181a, and their potential targets. Russ J Bioorg Chem. 2025;51(6):2443–54. https://doi.org/10.1134/S1068162024607018.
67. Pourasgar S, Ranji N, Asadpour L, Shahriarinour M, Nikpassand M. Antibacterial and anti-cancer properties of curcumin-functionalized silica-coated

Fe3O4 Magnetic nanoparticles. Arab J Sci Eng. 2025;50(9):6231–49. https://doi.org/10.1007/s13369-024-09273-2.
68. Rasaei M, Mohajeri E, Siahmazgi AS, Chegini SN, Dabirian S, Zahmatkesh H, et al. Design and synthesis of a novel indole derivative (2Cl-5N-ind-dione) and its effect on miR-181a, miR-200a, and miR-34a expression, targeting apoptosis, and migration pathways in HT-29 colorectal cancer cells. Russ J Bioorg Chem. 2025;51(6):2621–35. https://doi.org/10.1134/S1068162025600825.
69. Khakinezhad Tehrani F, Ranji N, Kouhkan F, Hosseinzadeh S. Apoptosis induction and proliferation inhibition by silibinin encapsulated in nanoparticles in MIA PaCa-2 cancer cells and deregulation of some miRnas. Iran J Basic Med Sci. 2020;23(4):469–82. https://doi.org/10.22038/ijbms.2020.39427.9349.
70. Fares J, Fares MY, Khachfe HH, Salhab HA, Fares Y. Molecular principles of metastasis: a hallmark of cancer revisited. Sig Transduct Target Ther. 2020;5(1):28. https://doi.org/10.1038/s41392-020-0134-x.
71. Mousavi Eshkelani SM, Kouchakinejad R, Dabirian S, Vakilinezami P, Shokrani K, Tajmehri H, et al. Anticancer activity of an apigenin-functionalized silica-coated silver oxide nanocomposite against human gastric adenocarcinoma cells (AGS): in vitro and in silico analysis. BMC Biotechnol. 2026;26(1). https://doi.org/10.1186/s12896-026-01118-0.
72. Al-Samydai A, Qaraleh MA, Alshaer W, Al-Halaseh LK, Issa R, Alshaikh F, et al. Preparation, characterization, wound healing, and cytotoxicity assay of PEGylated nanophytosomes loaded with 6-gingerol. Nutrients. 2022;14(23):5170. https://doi.org/10.3390/nu14235170.
73. Amin A, Farrukh A, Murali C, Soleimani A, Praz F, Graziani G, et al. Saffron and its Major ingredients' effect on colon cancer cells with mismatch repair deficiency and microsatellite instability. Molecules. 2021;26(13):3855. https://doi.org/10.3390/molecules26133855.
74. Saba R, Sorensen DL, Booth SA. MicroRNA-146a: a dominant, Negative regulator of the innate immune response. Front Immunol. 2014;5:578. https://doi.org/10.3389/fimmu.2014.00578.
75. Aslani MR, Armin F, Abedi A, Keramati E, Ghobadi H. Potential role of saffron and its components on miRNA levels in various disorders, a comprehensive review. Iran J Basic Med Sci. 2023;26(10):1120–30.
76. Su Y-F, Lin C-S, Shen P-C, Chuang S-E, Dai Y-H, Huang T-W, et al. MiR-34a functions as a tumor suppressor in oral cancer through the inhibition of the Axl/Akt/GSK-3β pathway. J Dent Sci. 2024;19(1):428–37. https://doi.org/10.1016/j.jds.2023.08.013.
77. Yu J, Qi J, Sun X, Wang W, Wei G, Wu Y, et al. MicroRNA-181a promotes cell proliferation and inhibits apoptosis in gastric cancer by targeting RASSF1A. Oncol Rep. 2018;40(4):1959–70. https://doi.org/10.3892/or.2018.6632.
78. Pakizehkar S, Ranji N, Naderi Sohi A, Sadeghizadeh M. Curcumin loaded PEG400-OA nanoparticles: a suitable system to increase apoptosis, decrease migration, and deregulate miR-125b/miR182 in MDA-MB-231 human breast cancer cells. Polym Adv Techs. 2020;31(8):1793–804. https://doi.org/10.1002/pat.4906.
79. Chen X, Yue W, Tian L, Li N, Chen Y, Zhang L, et al. A plant-based medicinal food inhibits the growth of human gastric carcinoma by reversing epithelial–mesenchymal transition via the canonical Wnt/β-catenin signaling pathway. BMC Complement Med Ther. 2021;21(1):137. https://doi.org/10.1186/s12906-021-03301-6.
80. Tehrani FK, Ranji N, Kouhkan F, Hosseinzadeh S. PANC-1 cancer stem-like cell death with silybin encapsulated in polymersomes and deregulation of stemness-related miRnas and their potential targets. Iran J Basic Med Sci. 2021;24(4):514–23. https://doi.org/10.22038/ijbms.2021.54001.12136.
81. Nakazato T, Ito K, Ikeda Y, Kizaki KMGT. Green tea component, catechin, induces apoptosis of human malignant B cells via Production of Reactive Oxygen Species. Clin Cancer Res. 2005;11(16):6040–49. https://doi.org/10.1158/1078-0432.CCR-04-2273.
82. Li W, Zhou Y, Yang J, Li H, Zhang H, Zheng P. Curcumin induces apoptotic cell death and protective autophagy in human gastric cancer cells. Oncol Rep. 2017;37(6):3459–66. https://doi.org/10.3892/or.2017.5637.
83. Biltekin SN, Karadag AE, Demirci F, Demirci B. In vitro anti-inflammatory and anticancer Evaluation of Mentha spicata L. and Matricaria chamomilla L. Essential Oils. Essent Oils. ACS Omega. 2023;8(19):17143–50. https://doi.org/10.1021/acsomega.3c01501.
84. Shaik NA, Al-Kreathy HM, Ajabnoor GM, Verma PK, Banaganapalli B. Molecular designing, virtual screening and docking study of novel curcumin analogue as mutation (S769L and K846R) selective inhibitor for EGFR. Saudi J Biol Sci. 2019;26(3):439–48. https://doi.org/10.1016/j.sjbs.2018.05.026.
85. Razak S, Afsar T, Bibi N, Abulmeaty M, Qamar W, Almajwal A, et al. Molecular docking, pharmacokinetic studies, and in vivo pharmacological study of indole derivative 2-(5-methoxy-2-methyl-1H-indole-3-yl)-N'-[(E)-(3-nitrophenyl) methylidene] acetohydrazide as a promising chemoprotective agent against cisplatin induced organ damage. Sci Rep. 2021;11(1):6245.
86. Uddin SMN, Rasool S, Geethakumari AM, Ahmed WS, Biswas KH. Engineering β-catenin-derived peptides for α-catenin binding. Emergent Mater. 2025;8(2):1183–97. https://doi.org/10.1007/s42247-024-00663-8.
87. Yan XE, Zhu SJ, Liang L, Zhao P, Choi HG, Yun CH. Structural basis of mutant-selectivity and drug-resistance related to CO-1686. Oncotarget. 2017;8(32):53508–17. https://doi.org/10.18632/oncotarget.18588.

Publisher's Note

Springer Nature remains neutral with regard to jurisdictional claims in published maps and institutional affiliations.